bioRxiv preprint doi: https://doi.org/10.1101/135699; this version posted May 9, 2017. The copyright holder for this preprint (which was not certified by peer review) is the author/funder, who has granted bioRxiv a license to display the preprint in perpetuity. It is made available under aCC-BY-NC-ND 4.0 International license.

3D single-molecule super-resolution microscopy with a tilted light sheet

Anna-Karin Gustavsson[1,2], Petar N. Petrov[1], Maurice Y. Lee[1,3], Yoav Shechtman[1,4] & W. E. Moerner[1,3,*]

[1]Department of Chemistry, Stanford University, Stanford, CA 94305, USA
[2]Department of Biosciences and Nutrition, Karolinska Institutet, Stockholm, SE-17177, Sweden
[3]Biophysics Program, Stanford University, Stanford, CA 94305, USA
[4]Present address: Biomedical Engineering Department, Technion, Israel Institute of Technology, Haifa 3200003, Israel
*e-mail: wmoerner@stanford.edu

Tilted light sheet microscopy with 3D point spread functions (TILT3D) combines a tilted light sheet illumination scheme and engineered point spread functions with axial ranges up to ten µm for low-background, 3D super-localization of single molecules. This system is built upon a standard inverted microscope and has minimal custom parts. The result is simple and flexible 3D super-resolution imaging with tens of nm localization precision throughout thick mammalian cells.

Several methods have been developed to extend the imaging capability of single-molecule super-resolution (SR) microscopy[1-3] to three dimensions (3D), including multiplane imaging, interferometric approaches, and point spread function (PSF) engineering (for a review, see [4]). In the case of PSF engineering, the axial position of a molecule is encoded in the shape of the PSF, and strategies include astigmatism[5] and the bisected pupil PSF[6] with axial ranges of 1-2 µm, self-bending[7] and double-helix (DH) PSFs[8-11]with axial ranges of ~2-3 µm, and the recently developed Tetrapod PSFs[12, 13] which have a tunable range of up to 20 µm. PSF engineering typically only requires the addition of a small number of optical elements to a standard microscope, making the method relatively simple to implement while exhibiting high precision for 3D single-molecule localization.

One method to improve the precision of single-molecule localization is to reduce the background coming from out-of-focus fluorophores by using light sheet illumination[14], where the sample is excited by a thin sheet of light orthogonal to the detection axis. Numerous light sheet designs have been implemented for SR imaging[15-20], but these designs have certain drawbacks such as being incompatible with imaging of fluorophores close to the coverslip using high numerical aperture (NA) imaging objectives[17, 18] or require complicated optical and electronic designs or many custom-made parts which are often expensive and difficult to build and operate, and thus may not be easily accessible to the general research community.

Here, we present TILT3D, an imaging platform that combines a novel, *tilted* light sheet illumination strategy with long axial range PSFs. We alleviate many of the aforementioned difficulties in existing light sheet designs by tilting the illumination plane; for example, two perpendicular objectives in close proximity are not required. TILT3D: (a) yields high localization precision of single molecules in 3D over the entire axial range of a mammalian cell via scanning of the light sheet combined with imaging with engineered PSFs, (b) has the usual light sheet advantages of reduced photobleaching and photodamage of the sample, but most importantly (c) is easy and cost-efficient to implement and operate. We validated TILT3D for 3D SR imaging in mammalian cells by imaging microtubules, mitochondria, and the full nuclear lamina using both DH and Tetrapod PSFs.

bioRxiv preprint doi: https://doi.org/10.1101/135699; this version posted May 9, 2017. The copyright holder for this preprint (which was not certified by peer review) is the author/funder, who has granted bioRxiv a license to display the preprint in perpetuity. It is made available under aCC-BY-NC-ND 4.0 International license.

In TILT3D, there is no need to spend considerable effort and expense producing an extremely thin light sheet, because the 3D positions of the single molecules are not determined from the position of the light sheet but instead from the shapes of the long axial range PSFs. Therefore, our tilted light sheet was simply created using a cylindrical lens, directed into a glass-walled sample chamber using a prism, and focused at the bottom of the sample chamber using a long working distance illumination objective (**Fig. 1a** and **Supplementary Fig. 1**). The long working distance allows the light sheet to be introduced without dipping the objective into the sample chamber, reducing the risk of sample contamination. The sample chamber can be left open to allow for easy sample access, or sealed to prevent sample contamination and evaporation of medium, and to limit access of oxygen to the sample. A 10° downward tilt of the light sheet enables the light sheet to be introduced into the sample chamber far away from the distorting bottom glass-water interface, while allowing focusing even at the bottom of a cell. The resulting light sheet has a thickness of 2.1 µm and width of 19 µm ($1/e^2$), and a confocal parameter of 73 µm (**Supplementary Fig. 2a, b**), making it well-suited for studies of mammalian cells. If needed, the light sheet can be scanned within the image plane and in the axial direction to section the cell using a motorized tiltable mirror positioned in the conjugate plane to the back aperture of the illumination objective (**Supplementary Figs. 2c** and **3**). The two illumination modes compared here (wide-field epi-illumination and light sheet) were easily toggled with a flip mirror.

A lens pair in 4*f* configuration was added to the emission side of the microscope to implement PSF engineering, i.e. phase modulation of the light in the Fourier plane of the microscope. Phase modulation was implemented using transmissive dielectric phase masks or a deformable mirror (DM) to create the 3D PSFs (**Fig. 1a** and **Supplementary Fig. 4**). The long axial range of these PSFs makes them well-suited for imaging with the 2-µm thick light sheet. The DH PSF consists of two lobes instead of just one, where the midpoint between the two lobes reports on the xy position and the z position is determined from the angular orientation of the line connecting the center of the lobes. The Tetrapod PSFs describe a more complex pattern, roughly tracing out the shape of a tetrapod when envisioned in 3D (**Fig. 1b**). A key advantage of the Tetrapod PSF is its smoothly varying phase pattern that can be generated with a DM, as demonstrated here for the first time, rather than using a microfabricated dielectric mask or an inherently photon inefficient liquid crystal spatial light modulator. The resulting PSFs are both photon efficient and easily tunable for different depth ranges.

Light sheet illumination was shown to yield up to a five-fold increase in the signal-to-background ratio (SBR) relative to conventional epi-illumination (**Fig. 1c**), resulting in improved localization precision for 3D imaging. The setup performance was benchmarked by 2D single-molecule imaging of lamin B1 in HeLa cells immunolabeled with Alexa Fluor 647, using a DM to generate a conventional clear aperture PSF for single-molecule detection in the middle of the nucleus and a 10-µm axial range Tetrapod PSF for interleaved detection of a fiducial bead at the coverslip (**Supplementary Fig. 5**, and **Supplementary Video 1**). This scheme (**Supplementary Fig. 6**) makes it easy to alternate the imaging of the nuclear lamina and the fiducial bead several µm below at the coverslip surface while keeping the focal plane stationary. The single molecules were excited at 647 nm using light sheet illumination, while the bright fiducial bead was excited at 561 nm using epi-illumination. Using different excitation wavelengths for the sample and the fiducial bead prevented the bright bead from saturating the camera pixels while keeping a high photon count (i.e. good localization precision) for proper 3D drift tracking. The fiducial bead was localized in real time and the sample drift was corrected in the axial direction via feedback to a piezoelectric objective scanner. Line scanning over the super-resolved structure yielded a measured lamina width of 130 nm (FWHM).

bioRxiv preprint doi: https://doi.org/10.1101/135699; this version posted May 9, 2017. The copyright holder for this preprint (which was not certified by peer review) is the author/funder, who has granted bioRxiv a license to display the preprint in perpetuity. It is made available under aCC-BY-NC-ND 4.0 International license.

Next, the 3D SR imaging capability of the Tetrapod PSFs was evaluated by imaging of microtubules in BS-C-1 cells immunolabeled with Alexa Fluor 647 (**Fig. 2a** and **Supplementary Videos 2-4**). A similar imaging methodology was used as for the 2D lamin B1 sample, with the exception that a 4-µm Tetrapod PSF was used for single-molecule detection and a 6-µm Tetrapod PSF was used for fiducial imaging. The analysis methodology used for Tetrapod PSFs is outlined in **Supplementary Fig. 7**. The average localization precision was estimated to be ~10 nm in xy and 15 nm in z (**Supplementary Fig. 8**).

To further demonstrate the versatility of the imaging platform, the DM was replaced by a transmissive DH dielectric phase mask for 3D SR imaging of the mitochondrial outer membrane in HeLa cells visualized by TOM20 immunolabeled with Alexa Fluor 647 (**Fig. 2b**, **Supplementary Fig. 9**, and **Supplementary Videos 5-7**). In this case, far red fiducial beads were used, allowing for continuous excitation using 647 nm and detection using the DH PSF. Cross-sections reveal the hollow structure of the mitochondrial outer membrane (**Fig. 2c** and **Supplementary Fig. 9**). This imaging scheme was very easy to implement and required no scripts to control the setup and only a single laser for illumination.

Mitochondria in HeLa cells were also imaged with the DH PSF when switching from epi-illumination to light sheet illumination to allow for direct comparison between the two illumination modes. This resulted in localization precisions when using epi/light sheet illumination of 23/16 nm in xy and 35/24 nm in z, respectively, demonstrating considerable improvement when using light sheet illumination (**Supplementary Fig. 10** and **Supplementary Video 8**).

Next, 3D SR imaging of the entire nuclear lamina in HeLa cells immunolabeled with Alexa Fluor 647 was performed using a similar scheme as for the 2D lamin B1 sample with interleaved illumination and live axial drift correction (**Fig. 2d**, **Supplementary Fig. 11**, and **Supplementary Movies 9-11**). In this case the 4*f* system was extended to two channels, where single molecules were detected using the DH PSF in the far red channel and the fiducial beads were detected in the red channel using a 6-µm Tetrapod PSF implemented using transmissive phase masks. The focal plane was moved together with the light sheet to sample the entire nuclear lamina in several thick, overlapping slices. The long axial range of the Tetrapod PSF allowed the fiducial beads to be detected and localized in all slices. At 3.3 µm above the coverslip, the localization precision was estimated to 16 nm in xy and 23 nm in z for SM detection using the DH PSF, and 3 nm in xy and 7 nm in z for fiducial bead detection using the 6-µm Tetrapod PSF (**Supplementary Fig. 12a, b**). The thickness of the lamina at the bottom and the top of the cell were measured to be 113 nm and 101 nm (FWHM), respectively (**Supplementary Fig. 12c**). An xz view reveals the lamina meshwork enveloping an intranuclear lamina channel (**Fig. 2d**, **Supplementary Movie 12**).

By combining a tilted light sheet with PSF engineering, TILT3D offers a simple yet powerful tool for 3D SR imaging in whole mammalian cells using only a few axial light sheet positions. No scanning of the detection objective is required over the entire range of the PSF. The flexible design allows for imaging close to a conventional coverslip using a high NA detection objective and easy switching between illumination modes, lasers, and PSFs. We demonstrate for the first time 3D SR imaging using the Tetrapod PSF family, which have a useful range of up to 10 µm in this work. The platform can be extended to multi-color light sheet imaging and to more advanced light sheet techniques such as a scanned Gaussian, Bessel[21], or Airy beams[22] by replacing the motorized mirror with an acousto-optical deflector or a spatial light modulator. Furthermore, the DM can be used for adaptive optics to correct system aberrations[23]. We believe that TILT3D in the future will become an important tool not only for 3D SR imaging, but also for live whole-cell single-particle and single-molecule tracking.

METHODS

bioRxiv preprint doi: https://doi.org/10.1101/135699; this version posted May 9, 2017. The copyright holder for this preprint (which was not certified by peer review) is the author/funder, who has granted bioRxiv a license to display the preprint in perpetuity. It is made available under aCC-BY-NC-ND 4.0 International license.

Methods, including statements of data availability and any associated references, are available in the online version of the paper.

ACKNOWLEDGMENTS

This work was supported in part by the National Institute of General Medical Sciences (Grant No. R35GM118067) to W.E.M. and by the National Institute of Biomedical Imaging and Bioengineering (Grant No. U01EB021237) to W.E.M. A.-K.G. acknowledges partial financial support from the Swedish Research Council (Grant No. 2016-00130), and from the Foundation BLANCEFLOR Boncompagni-Ludovisi, née Bildt. M.Y.L. is supported by a National Science Scholarship (PhD) from A*STAR, Singapore. Y.S. is supported in part by a Career Advancement Chairship from the Technion. The authors also thank Dr. Carl G. Ebeling, Worldwide Application Scientist for Bruker Fluorescence Microscopy, for his support and for the use of the Bruker SRX visualization and analysis software for rendering localization data, and Dr. Steffen Sahl for early discussions. Fabrication of dielectric phase masks was performed at the Stanford Nanofabrication Facility, which is supported by the National Science Foundation as part of the National Nanotechnology Coordinated Infrastructure under award ECCS-1542152.

AUTHOR CONTRIBUTIONS

A.-K.G., P.N.P., and M.Y.L. developed and constructed the imaging platform. A.-K.G. labeled the cells, planned and performed the experiments, and analyzed the 2D and double-helix data. P.N.P. and M.Y.L. helped performing the experiments. P.N.P. and Y.S. developed the Tetrapod analysis algorithms and P.N.P. analyzed the Tetrapod data. M.Y.L. fabricated the transmissive Tetrapod phase mask. Y.S. developed the Tetrapod phase patterns and assisted with their implementation on the deformable mirror. W.E.M. conceived the idea and supervised the research. All authors contributed to writing the paper.

COMPETING FINANCIAL INTERESTS

The authors declare no competing financial interests.

REFERENCES

1. Betzig, E. *et al*. *Science* **313**, 1642-1645 (2006).
2. Hess, S. T., Girirajan, T. P. K. & Mason, M. D. *Biophys. J.* **91**, 4258-4272 (2006).
3. Rust, M. J., Bates, M. & Zhuang, X. *Nat. Methods* **3**, 793-796 (2006).
4. von Diezmann, A., Shechtman, Y. & Moerner, W. E. *Chem. Rev.* (2017).
5. Huang, B., Jones, S. A., Brandenburg, B. & Zhuang, X. *Nat. Methods* **5**, 1047-1052 (2008).
6. Backer, A. S., Backlund, M. P., Diezmann, A. R., Sahl, S. J. & Moerner, W. E. *Appl. Phys. Lett.* **104**, 193701-193705 (2014).
7. Jia, S., Vaughan, J. C. & Zhuang, X. *Nat. Photonics* **8**, 302-306 (2014).
8. Pavani, S. R. P. *et al*. *Proc. Natl. Acad. Sci. U. S. A.* **106**, 2995-2999 (2009).
9. Thompson, M. A., Lew, M. D., Badieirostami, M. & Moerner, W. E. *Nano Lett.* **10**, 211-218 (2010).
10. Lew, M. D. *et al*. *Proc. Natl. Acad. Sci. U. S. A.* **108**, E1102-E1110 (2011).
11. Carr, A. R. *et al*. *Biophys. J.* **112**, 1444-1454 (2017).
12. Shechtman, Y., Sahl, S. J., Backer, A. S. & Moerner, W. E. *Phys. Rev. Lett.* **113**, 133902 (2014).
13. Shechtman, Y., Weiss, L. E., Backer, A. S., Sahl, S. J. & Moerner, W. E. *Nano Lett.* **15**, 4194-4199 (2015).
14. Huisken, J., Swoger, J., Del Bene, F., Wittbrodt, J. & Stelzer, E. H. *Science* **305**, 1007-1009 (2004).
15. Galland, R. *et al*. *Nat Meth* **12**, 641-644 (2015).
16. Chen, B. C. *et al*. *Science* **346**, 1257998 (2014).
17. Gebhardt, J. C. *et al*. *Nat. Methods* **10**, 421-426 (2013).
18. Zanacchi, F. C. *et al*. *Nat. Methods* **8**, 1047-1049 (2011).
19. Meddens, M. M. *et al*. *Biomed. Opt. Express* **7**, 2219-2236 (2016).

bioRxiv preprint doi: https://doi.org/10.1101/135699; this version posted May 9, 2017. The copyright holder for this preprint (which was not certified by peer review) is the author/funder, who has granted bioRxiv a license to display the preprint in perpetuity. It is made available under aCC-BY-NC-ND 4.0 International license.

20. Hu, Y. *et al*. *Optical Nanoscopy* **2**, 7 (2013).
21. Planchon, T. A. *et al*. *Nat. Methods* **8**, 417-423 (2011).
22. Vettenburg, T. *et al*. *Nat. Methods* **11**, 541-544 (2014).
23. Burke, D., Patton, B., Huang, F., Bewersdorf, J. & Booth, M. *Optica* **2**, 177-185 (2015).

bioRxiv preprint doi: https://doi.org/10.1101/135699; this version posted May 9, 2017. The copyright holder for this preprint (which was not certified by peer review) is the author/funder, who has granted bioRxiv a license to display the preprint in perpetuity. It is made available under aCC-BY-NC-ND 4.0 International license.

ONLINE METHODS

Optical setup. In this work, the optical setup was built around a conventional inverted microscope (IX71, Olympus) (**Fig. 1a** and **Supplementary Fig. 1**). Illumination lasers (405 nm, 100 mW; 561 nm, 200 mW; and 647 nm, 120 mW, all Coherent) were spectrally filtered (561 nm: ff01-554/23-25 excitation filter, 647 nm: ff01-631/36-25 excitation filter, both Semrock), circularly polarized (LPVISB050-MP2 polarizers, Thorlabs, and 405 nm: Z-10-A-.250-B-405 quarter-wave plate, Tower Optical, 561 nm: WPQ05M-561 quarter-wave plate, Thorlabs, 647 nm: WPQ05M-633 quarter-wave plate, Thorlabs), and expanded and collimated using lens telescopes. The toggling of the lasers was controlled with shutters (VS14S2T1 with VMM-D3 three-channel driver, Vincent Associates Uniblitz) and synchronized with the detection optics via MATLAB. The 405 nm and 561 nm lasers were introduced into the back port of the microscope through a Köhler lens to allow for wide field epi-illumination. The 647 nm laser was either introduced into the epi-illumination pathway or sent to the light sheet illumination pathway; the pathway was easily switched with a flip mirror. The light sheet illumination pathway consisted of a cylindrical lens (LJ1558L2-A, f = 300 mm, Thorlabs, or ACY254-200-A, f = 200 mm, Thorlabs), which focused the light in only one dimension onto a motorized mirror (8821 mirror mount with 8742 Picomotor controller, Newport). The motorized mirror plane was imaged onto the back aperture of a long working distance illumination objective (378-803-3, 10x, NA 0.28, Mitutoyo) by two lenses in a 4f configuration. The illumination objective then focused the light sheet, which was directed into the sample chamber (704-00-20-10, Hellma) at an angle of about 10° using a glass prism (PS908L-A, Thorlabs). The long working distance of the illumination objective allowed for introduction of the light sheet without dipping the objective into the sample chamber, reducing the risk of sample contamination. The 10° tilt of the illumination pathway into the sample chamber allowed the light sheet to be focused close to the coverslip surface, while preventing the beam profile from being aberrated by passage through the bottom glass-water interface. The entire light sheet illumination path was mounted on a bread board moved by an xyz translation stage (460P, Newport).

The emitted light from the fluorophores was detected by a high NA detection objective (UPLSAPO100XO, 100x, NA 1.4, Olympus) mounted on a piezoelectric objective scanner (Nano-F100, C-Focus, Mad City Labs), spectrally filtered (Di01-R405/488/561/635 dichroic, for far red detection: Semrock, ET700/75m bandpass filter, Chroma, ZET647NF notch filter, Chroma, 3RD650LP longpass filter, Omega Optical, and for red detection: ZET647NF notch filter, Chroma, et610/60 bandpass filter, Chroma, and FF01-593/40 bandpass filter, Semrock), and focused by the microscope tube lens, before entering a 4f imaging system. The first lens of the 4f system (f = 150 mm when using a deformable mirror and f = 90 mm when using transmissive phase masks) was positioned one focal length from the intermediate image plane formed by the microscope tube lens. In the plane one focal length after the first 4f lens (i.e., the Fourier plane of the imaging path), the phase of the emitted light was modulated to reshape the point spread function (PSF) to encode the axial position of the emitter. After phase modulation, the light was focused by the second 4f lens and imaged using an EM-CCD camera (iXon3 897, Andor). To create a two-channel 4f system (**Fig. 1a**, top right inset) a dichroic mirror (T660lpxrxt, Chroma) was inserted before the phase masks to transmit far red light into the first light path and reflect light with wavelengths shorter than 660 nm into a second light path. The paths were merged before the camera using a D-shaped mirror (BBD1-E02, Thorlabs). The desired phase pattern was implemented either using transmissive dielectric phase masks (for the DH mask, Double-Helix Optics, LLC, and the Tetrapod phase mask was fabricated as outlined in section **Fabrication of transmissive Tetrapod phase mask**), or using a deformable mirror (DM) (Multi-DM 3.5, Boston Micromachines Corporation). When the transmissive phase masks were used, the physical mask had to be exchanged whenever there was an adjustment to be made to the desired working

bioRxiv preprint doi: https://doi.org/10.1101/135699; this version posted May 9, 2017. The copyright holder for this preprint (which was not certified by peer review) is the author/funder, who has granted bioRxiv a license to display the preprint in perpetuity. It is made available under aCC-BY-NC-ND 4.0 International license.

axial range of the PSF and/or the wavelength of the emitted light. To facilitate these exchanges, the transmissive phase masks were mounted on magnetic mounts. When the DM was used, the phase pattern was controlled from a computer and could be rapidly updated with different phase patterns to produce PSFs with different axial ranges and/or at different wavelengths of light. Another common way to implement the phase pattern is to use a spatial light modulator (SLM). However, replacing the SLM with a transmissive phase mask or a DM substantially increases photon efficiency, which is a limiting factor for obtaining better precision for single-molecule imaging. The loss of the unmodulated polarization with a liquid-crystal SLM can, however, be recovered[24]. The active regions of the transmissive masks and the DM had diameters of 2.7 mm and 4.2 mm, respectively. To ensure that the electric field diameter at the Fourier plane, d_E, matched the diameter of the active regions, the focal lengths of the 4*f* lenses, f_{4f}, had to be chosen accordingly. Under the Abbe sine condition, the electric field diameter depends on the focal length according to

$$d_E = \frac{2 f_{4f} NA}{\sqrt{M^2 - NA^2}}, \tag{1}$$

where NA = 1.4 is the numerical aperture of the detection objective and M = 100 is the magnification of the microscope. Choosing focal lengths of the 4*f* lenses of 90 mm and 150 mm for the transmissive masks and DM, respectively, resulted in electric field diameters of 2.5 mm and 4.2 mm, which matched or were slightly smaller than the active mask regions. Overfilling the mask would lead to unmodulated light in the image plane.

Light sheet characterization. The width, r, and thickness, ω_0, of the light sheet were determined from directly imaging the excitation beam propagating through a fluorescent solution (1:1000 Alexa Fluor 647 conjugated secondary antibodies (ab150067, Abcam) in water). The thickness was measured after rotating the cylindrical lens by 90°. The cross-sectional profiles of the light sheet were measured by drawing a line perpendicular to the axis of light propagation across the resulting images and fitting the pixel intensities with a 1D Gaussian function. The thickness and width of the light sheet were determined to be 2.1 µm and 18.7 µm ($1/e^2$), respectively (**Supplementary Fig. 2a**). These parameters can be compared to the theoretically expected values of the width, r,

$$r = r_0 \frac{f_1}{f_{cyl}} \frac{f_{obj}}{f_2}, \tag{2}$$

and the thickness, ω_0,

$$\omega_0 = \frac{\lambda}{\pi \tan^{-1}\left(\frac{R}{f_{obj}}\right)}, \tag{3}$$

where r_0 = 1.1 mm is the (measured) beam radius ($1/e^2$) before the cylindrical lens, and f_{cyl} = 300 mm, f_1 = 35 mm, f_2 = 125 mm, and f_{obj} = 20 mm are the focal lengths of the cylindrical lens, the first and second lens in the illumination 4*f* system, and the illumination objective lens, respectively, λ = 0.647 µm is the wavelength of the excitation laser, and

$$R = r_0 \frac{f_2}{f_1} \tag{4}$$

bioRxiv preprint doi: https://doi.org/10.1101/135699; this version posted May 9, 2017. The copyright holder for this preprint (which was not certified by peer review) is the author/funder, who has granted bioRxiv a license to display the preprint in perpetuity. It is made available under aCC-BY-NC-ND 4.0 International license.

is the radius of the beam ($1/e^2$) at the back aperture of the illumination objective in the axis not being focused by the cylindrical lens. By inserting these values of the various parameters into the formulas, the theoretical width and thickness were calculated to be 21.5 µm and 1.0 µm ($1/e^2$) respectively. While the theoretical width agrees reasonably well with the measured width, the discrepancy between the theoretical (1.0 µm) and measured thicknesses (2.1 µm) may be caused by scattering within the sample chamber or by imperfections of the illumination objective lens. In addition, in the current alignment of the optical setup, the back aperture of the objective is almost fully filled, i.e. R is not much smaller than the back aperture radius of the illumination objective lens. This means that the assumption used in equation 3 that the half cone angle of the light, θ, can be expressed as $\tan\theta = R/f_{obj}$ might not be completely accurate.

By using Gaussian beams, there is an inherent tradeoff between the depth of focus, or the confocal parameter, b, and the thickness of the light sheet. This is evident from the theoretical relation between b and ω_0:

$$b = \frac{2\pi\omega_0^2}{\lambda}, \tag{5}$$

which shows that b scales with ω_0 squared. Using extremely thin light sheets thus limits the useful field of view that can be imaged. To estimate the confocal parameter of our light sheet, we decreased the tilt of the beam and imaged the beam profile using an imaging objective with 20x magnification (1-UB525, 20x, NA 0.5, Olympus). We then used the Gaussian beam propagation equation to fit the thickness of the light sheet, ω, as a function of the position x along the direction of beam propagation as measured from the focus,

$$\omega(x) = \omega_0\sqrt{1+\left(\frac{x}{z_R}\right)^2}. \tag{6}$$

Here z_R is the Rayleigh length, which relates to the confocal parameter as $b = 2z_R$. Fitting the data using this equation allowed us to experimentally determine z_R = 36.7 µm and ω_0 = 2.5 µm for the light sheet (**Supplementary Fig. 2b**). Inserting ω_0 = 2.5 µm into equation 5 results in a theoretical confocal parameter of 60.7 µm, corresponding to a theoretical Rayleigh length of 30.4 µm. This is in reasonable agreement with our data. The corresponding theoretical confocal parameter for a beam with ω_0 = 2.1 µm is 42.8 µm. These calculations show that our light sheet beam can be described using the Gaussian beam propagation equation, and that the light sheet has a usable range of more than 40 µm in the direction of propagation of the light sheet. This allows for measurements of most features of interest in mammalian cells without scanning of the sample. Measuring the *y* width of the light sheet across a range of 340 µm in the direction of beam propagation resulted in an experimental value of 19.1±0.1 µm, demonstrating that the width remains relatively constant across the entire field of view. All fits were performed with a non-linear least square algorithm in MATLAB.

The light sheet was tilted by positioning the illumination objective and the lens and mirror just before it such that the light path was inclined by about 10° with respect to the vertical (**Supplementary Fig. 1**). The resulting tilt of 10° with respect to the horizontal in the sample chamber was measured from the side of the chamber when propagating the light sheet beam through a fluorescent solution (1:1000 Alexa Fluor 647 conjugated secondary antibodies (ab150067, Abcam) in water). This tilt allowed the light sheet to be introduced into the sample chamber far above the aberrating interface of the bottom coverslip. In addition, the light sheet could still be focused all the way to the coverslip which is useful for imaging the

bioRxiv preprint doi: https://doi.org/10.1101/135699; this version posted May 9, 2017. The copyright holder for this preprint (which was not certified by peer review) is the author/funder, who has granted bioRxiv a license to display the preprint in perpetuity. It is made available under aCC-BY-NC-ND 4.0 International license.

entirety of adherent cells. The tilt will cause the light sheet to illuminate one side of the cell about 2-3 µm higher up than the other side. However, this is not a problem when combining the light sheet illumination with long axial range PSFs, since any fluorescent molecule within the entire illuminated range will be detected. It is important to highlight that the absolute axial position of each single-molecule emitter is encoded in the shape of the PSF rather than in the position (or thickness) of the light sheet.

Translation of light sheet using a motorized mirror. Translation of the light sheet in the lateral and axial direction in the sample chamber was achieved by tilting a 2D motorized mirror (8821 mirror mount with 8742 Picomotor controller, Newport) positioned in a conjugate plane to the back aperture of the illumination objective. The specifications of the motorized mirror for the maximum and minimum tilt angles are $\theta_{max} = 5°$ and $\theta_{min} = 4 \cdot 10^{-5}$ °, respectively. The theoretical maximum and minimum displacements, Δ, in the sample plane can be calculated according to following equation:

$$\Delta = f_1 \tan\theta \frac{f_{obj}}{f_2}. \tag{7}$$

By inserting the setup parameters into equation 7, the maximum and minimum displacements are calculated to be Δ_{max} = 490 µm and Δ_{min} = 3.9 nm. These calculations were experimentally validated by imaging the light sheet propagating through a fluorescent solution (1:1000 Alexa Fluor 647 conjugated secondary antibodies (ab150067, Abcam) in water) while moving the motorized mirror in steps each spanning 1000 θ_{min}. At each position, the fluorescence caused by the light sheet was imaged for 45 frames (50 ms per frame). The center and width of the light sheet were determined by fitting the cross-sectional profile in each frame with a 1D Gaussian function and calculating the average of those 45 positions. The measured displacement was calculated as the difference between the mean positions of the center of the light sheet at each step. These measurements resulted in a displacement, Δ_{meas}= 4.45 ± 0.11 µm per step (consisting of 1000 θ_{min}). This is in good agreement with the theoretical value of 3.9 µm per 1000 θ_{min} step (**Supplementary Figs. 2b** and **3**).

The total time required to complete a full step (1000 θ_{min}) was measured to 0.56 ± 0.02 s. During a total scan of 45 µm, the *y* width of the light sheet was measured to 17.8 ± 0.6 µm ($1/e^2$), showing that the width remained relatively constant across the scanned field of view.

Prism and sample chamber assembly. The glass prism was attached to a standard microscope stage using a custom-made right triangular aluminum prism for support. This is the only custom-made component of the entire imaging platform (other than the Tetrapod phase mask). The aluminum support was cut from a square aluminum bar and designed such that when the glass prism was attached to it, the back surface of the glass prism was exposed to air (instead of aluminum) to facilitate total internal reflection at the glass-air interface (**Supplementary Fig. 1b**). The aluminum prism was attached to the stage and the glass prism to the aluminum support using two-part silicone rubber (Ecoflex® 5, Reynolds Advanced Materials). The sample chamber was assembled by attaching a glass coverslip (Fisher Premium Cover Glass, no. 1.5) with cells cultured on it to the bottom of the four transparent polished walls of a sliced commercial glass cuvette (704-000-20-10, Hellma) using the two-part silicone rubber. Using a standard glass coverslip allowed for easy cell culturing and handling, and facilitated the usage of a high NA detection objective for super-resolution (SR) imaging. During imaging, the sample chamber could be left open on the top to allow for easy sample access, or it could be easily sealed by placing a second coverslip on top of the four walls and seal it with silicone rubber. This reduced the risk of sample contamination, decreased the rate of evaporation

bioRxiv preprint doi: https://doi.org/10.1101/135699; this version posted May 9, 2017. The copyright holder for this preprint (which was not certified by peer review) is the author/funder, who has granted bioRxiv a license to display the preprint in perpetuity. It is made available under aCC-BY-NC-ND 4.0 International license.

of the medium, and limited the access of oxygen to the sample. The glass surfaces between the coverslip and the imaging objective, and between the sample chamber and the glass prism, were brought into optical contact with immersion oil (Zeiss Immersol 518 F, n = 1.518). Clearly, index matching gel could also be used between the sample chamber and the glass prism. After imaging, the bottom coverslip could be removed and the chamber walls cleaned and reused.

Engineered point spread functions for 3D single-molecule localization. To obtain a complete picture of subcellular structures, cells must be imaged in all three dimensions (3D). There are several ways to achieve this[4]. Point scanning methods such as confocal microscopy[25] can yield 3D information with good contrast, but are inherently limited in resolution by diffraction. Another approach is multiplane imaging[26-28]. This method requires simultaneous acquisition of multiple images, and was reported to be applicable to an axial range of about 4 µm by scanning of the focal plane through the sample[28]. A third approach is to use interferometry[29, 30], which can result in very high localization precision. However, these setups are often rather complex and sensitive to small misalignments. They also require displacing the image plane for imaging of samples thicker than ~1.2 µm. In this work, we use a powerful approach that allows for scan-free wide field imaging over a several µm axial range. The strategy is to modify the shape of the PSF of the microscope to encode information about the axial (z) position of the single emitter, which is accomplished by modifying the phase pattern of the emitted light in the Fourier plane of the microscope. This method has been used to create the bisected pupil PSF[6], the corkscrew PSF[31], the self-bending PSF[7], the double-helix (DH) PSF[8-11], and the Tetrapod PSFs[12, 13]. The working axial ranges are ~1-2 µm for the bisected pupil PSF, ~2-3 µm for the corkscrew, self-bending, and DH PSFs, and tunable up to 20 µm for the Tetrapod PSFs.

In this work, we have used the DH PSF and the Tetrapod PSFs. These PSFs can precisely determine the 3D position of single molecules over entire cellular structures without requiring an extremely thin light sheet for illumination (**Fig. 1b** and **Supplementary Fig. 4**). Since the light sheet we use has an axial thickness near 2 µm, only a small number of axial sheet positions are required to image the full cell thickness. The phase pattern encoding for the DH PSF varies rapidly across the pupil plane and was implemented using a transmissive dielectric phase mask (Double-Helix Optics, LLC). The recently developed Tetrapod PSFs contain more complex patterns, roughly tracing out the shape of a tetrapod when envisioned in 3D (**Fig. 1b**). They have been designed and optimized to be maximally informative over a specified signal, background, and axial range using Fisher information to find the best superposition of Zernike polynomials to form their phase pattern. The Tetrapod PSFs have previously been used for tracking of single particles[13], but this work is the first demonstration of using the Tetrapod PSFs for single-molecule 3D SR imaging. The maximized information content of the PSFs in combination with the tunability of their axial range and design wavelength makes them extremely useful for imaging of cellular structures with different axial extent using fluorophores with various emission spectra. Since the Tetrapod phase patterns are smoothly varying, they can be implemented using a DM, as well as a transmissive mask or SLM. In this work, Tetrapod PSFs with 4 µm and 10 µm axial ranges and a design wavelength of 660 nm were implemented using a DM. Tetrapod PSFs with 6 µm axial range were implemented with both a DM and a transmissive phase mask. The 4-µm range PSF was used for single-molecule imaging, while the 6-µm and 10-µm range PSFs were used for imaging of bright fiducial beads. The long-axial range PSFs cover a larger transverse spatial extent than the standard PSF, which increases the demand for high SBR. Here this is solved by using light sheet illumination for single-molecule imaging. The large transverse spatial extent also requires the density of emitters to be sparser than for 2D imaging with the standard PSF. This can be achieved by initially forcing a larger fraction of the fluorophores into a dark state.

bioRxiv preprint doi: https://doi.org/10.1101/135699; this version posted May 9, 2017. The copyright holder for this preprint (which was not certified by peer review) is the author/funder, who has granted bioRxiv a license to display the preprint in perpetuity. It is made available under aCC-BY-NC-ND 4.0 International license.

Fabrication of transmissive Tetrapod phase mask. Transmissive dielectric 6-µm Tetrapod phase masks were fabricated using standard photolithography methods at the Stanford Nanofabrication Facility. Amorphous quartz wafers (4-inch diameter, ~475 µm in thickness, WRS Materials) were cleaned in a chemical bath of Piranha solution (90% sulfuric acid, 10% hydrogen peroxide) at 70°C for 20 min. The wafers were then rinsed with clean water in an automatic dump rinser and a spin/rinse dryer. Next, the wafers were placed in a Yield Engineering Systems (YES) oven to be dehydrated at 150°C before being primed with hexamethyldisilazane (HDMS) at 70°C for 20 min. After being primed, the wafers were spin-coated with a 1.6-µm thick layer of Shipley 3612 positive photoresist with a 5-mm edge bead removal by using a Silicon Valley Group (SVG) resist coat system. Any excess solvent was driven off by baking the wafers on a hot plate at 90°C for 120 seconds. Patterning of the photoresist film was done with a KarlSuss MA-6 aligner and the photoresist film was exposed to ultraviolet (UV) illumination for 1.6 seconds. The patterns on the binary masks used in this exposure step were created by converting the designed Tetrapod phase mask into three different binary masks (3 bits = 8 levels) with diameters of 2.7 mm. A vendor was used to print these binary mask patterns. To set the photoresist after the UV exposure, the wafers were baked on a hotplate at 110°C for 90 seconds. The positive photoresist in the UV-exposed regions was then removed by using a standard procedure on the SVG developer. Next, to drive off moisture and harden the remaining photoresist, the wafers were placed in a 90°C oven for 20 min. The etching of the quartz wafers was carried out with an Applied Materials Precision 5000 Etcher with the magnetically-enhanced reactive ion etch (MERIE) system. The duration of each etching period was calibrated and adjusted for each of the three etch steps. After the etch step, any photoresist left on the wafers was stripped with a Gasonics aura plasma asher. To be sure that any remaining photoresist was removed, the wafers were placed in a chemical bath of PRS-3000 at 60°C for 20 min. The etched and cleaned wafers were then rinsed with clean water in an automatic dump rinser and a spin/rinse dryer. After stripping any remaining photoresist, the 3D surface profiles of the phase masks on the quartz wafers were characterized with a Sensofar S Neox 3D optical profiler. This tool uses white-light vertical scanning interferometry to measure the step heights. After measuring the step heights, this entire conventional lithography process is repeated, starting with priming the clean and etched quartz wafers with HDMS again until all three etch steps were completed with the three different binary masks. Finally, after all three etch steps had been completed and measured, the Tetrapod phase masks were cut out of the 4-inch quartz wafer with a DISCO wafer saw.

Cell culture and seeding. HeLa and BS-C-1 cells were cultured at 37°C and 5% CO_2 in high-glucose Dulbecco's modified Eagle's medium (DMEM, HyClone) supplemented with 10% (v/v) FBS (HyClone). Two days before imaging, cultured cells were plated onto plasma-etched coverslips (Fisher Premium Cover Glass, no. 1.5) spun coat with a 1% (w/v) polyvinyl alcohol (PVA, Polysciences Inc.) layer containing red (lamin B1 and microtubules) (580/605 nm, F8810, Invitrogen) or far red (mitochondria) (625/645 nm, F8806, Invitrogen) fluorescent microspheres, cultured for 24 hours in high-glucose DMEM supplemented with 10% FBS, and subsequently cultured for 24 hours in high-glucose, phenol-red free DMEM (HyClone) supplemented with 10% FBS. During this period, some of the microspheres were endocytosed.

Cell fixation and immunolabeling. Immunolabeling steps were performed with coverslips placed on parafilm, while all other steps were performed with coverslips placed in 6-well plates. After the immunolabeling, all samples were protected from light and stored in PBS (HyClone) at 4°C. The samples were imaged within 48 hours of labeling.

bioRxiv preprint doi: https://doi.org/10.1101/135699; this version posted May 9, 2017. The copyright holder for this preprint (which was not certified by peer review) is the author/funder, who has granted bioRxiv a license to display the preprint in perpetuity. It is made available under aCC-BY-NC-ND 4.0 International license.

For lamin B1 labeling, HeLa cells (CCL-2, ATCC) were washed three times in PBS, fixed in chilled 4% paraformaldehyde (PFA) (Electron Microscopy Sciences) in PBS for 20 min, washed once in PBS, and incubated with 10 mM NH_4Cl (Sigma-Aldrich) in PBS for 10 minutes. Next, the cells were permeabilized with three washing steps with 0.2% (v/v) Triton X-100 (Sigma-Aldrich) in PBS with 5 min incubation between each wash, and blocked with 3% (w/v) BSA (Sigma-Aldrich) in PBS for 1 hour. The cells were then labeled with primary rabbit anti-lamin B1 (ab16048, Abcam) using a 1:1000 dilution in 1% (w/v) BSA in PBS for 2 hours, washed three times with 0.1% (v/v) Triton X-100 in PBS with 3 min incubation between each wash, and labeled with secondary donkey anti-rabbit conjugated with Alexa Fluor 647 (ab150067, Abcam) using a 1:1000 dilution in 1% (w/v) BSA in PBS for 1 hour. The cells were finally washed five times with 0.1% (v/v) Triton X-100 in PBS with 1 min incubation between each wash.

For immunolabeling of microtubules, BS-C-1 cells (CCL-26, ATCC) were washed three times in PBS, fixed in chilled 4% PFA in PBS for 20 min, washed once in PBS, and incubated with 10 mM NH_4Cl in PBS for 10 min. Next, the cells were permeabilized with three washing steps with 0.2% (v/v) Triton X-100 in PBS with 5 min incubation between each wash, and blocked with 3% (w/v) BSA in PBS. The cells were labeled with Alexa Fluor 647-conjugated primary rabbit anti-tubulin (ab59680, Abcam) using a 1:100 dilution in 1% (w/v) BSA in PBS for 2 hours, and then washed five times with 0.1% (v/v) Triton X-100 in PBS with 3 min incubation between each wash.

For immunolabeling of mitochondria, HeLa cells (CCL-2, ATCC) were washed two times in PBS, fixed in chilled 4% PFA in PBS for 20 min, washed once in PBS, and incubated with 10 mM NH_4Cl in PBS for 10 min. Next, the cells were permeabilized with three washing steps with 0.2% (v/v) Triton X-100 in PBS with 5 min incubation between each wash, and blocked with 3% (w/v) BSA in 0.1% (v/v) Triton X-100 in PBS for 1 hour. The cells were labeled with Alexa Fluor 647-conjugated primary rabbit anti-TOMM20 (ab209606, Abcam) using a 1:100 dilution in 1% (w/v) BSA in 0.1% (v/v) Triton X-100 in PBS for 2 hours. The cells were then washed five times with 0.1% (v/v) Triton X-100 in PBS with 3 min incubation between each wash, post-fixed in 4% PFA in PBS for 5 min, and washed three times in PBS.

Single-molecule super-resolution imaging. For diffraction-limited imaging, cells were imaged in PBS using low power 647 nm excitation (~1 W/cm^2). Comparisons between light sheet and epi-illumination were performed by manually switching illumination light paths using a flip mirror during image acquisition. Custom scripts were written in MATLAB to synchronize the laser shutters, phase patterns on the DM, image acquisition on the camera, and translation by the piezoelectric objective scanner. Scanning of the light sheet was performed using the New Focus Picomotor Application software (Newport).

For single-molecule SR imaging, the PBS was replaced by a reducing and oxygen-scavenging buffer[32] comprising 100 mM Tris-HCl (Invitrogen), 10% (w/v) glucose (BD Difco), 2 µl/ml catalase (Sigma-Aldrich), 560 µg/ml glucose oxidase (Sigma-Aldrich), and cysteamine (Sigma-Aldrich) with a concentration of 10 mM (Alexa Fluor 647 immunolabeled lamin B1 (2D) and microtubules), 20 mM (Alexa Fluor 647 immunolabeled mitochondria), or 40 mM (Alexa Fluor 647 immunolabeled lamin B1 (3D)). At the beginning of the measurement, a large fraction of the Alexa Fluor 647 molecules were converted into a dark state using 647 nm epi-illumination at 5 kW/cm^2. For all single-molecule measurements, an exposure time of 50 ms and a calibrated EM gain of 186 was used. For each imaging experiment, at least 300 dark frames were acquired when the shutter of the camera was closed. The mean of these dark frames was subtracted from the images before analysis. When using 3D PSFs, calibration of each PSF was carried out by axial scanning of the fiducial beads in the sample over the full PSF range using the piezoelectric objective scanner.

bioRxiv preprint doi: https://doi.org/10.1101/135699; this version posted May 9, 2017. The copyright holder for this preprint (which was not certified by peer review) is the author/funder, who has granted bioRxiv a license to display the preprint in perpetuity. It is made available under aCC-BY-NC-ND 4.0 International license.

For acquisition of 2D SR images of lamin B1 in HeLa cells, a 4*f* system with a DM was used for phase modulation in the imaging pathway. A standard PSF was used together with ~25 kW/cm^2 647 nm light sheet illumination for imaging of single Alexa Fluor 647 molecules, while for every twentieth frame a fiducial bead at the cover slip was imaged using a 10-µm Tetrapod PSF and 10 W/cm^2 561 nm epi-illumination (**Supplementary Fig. 6**). This scheme makes it easy to alternate the imaging of the nuclear lamina and of the fiducial bead several microns below at the surface of the coverslip while keeping the focal plane stationary. Using a fluorecent bead that is excited by a different wavelength reduced the risk of photobleaching the fluorophores and of saturating the single-molecule image by light from the fiducial bead, while maintaining a high photon count for the fiducial. The fiducial frame was analyzed in real time and the sample drift corrected in the axial direction via feedback to the piezoelectric objective scanner. The removal of axial drift prevented different horizontal sections of the cell from being imaged and superimposed over each other over the course of the measurement, which would have caused an apparent broadening of the lamina in the 2D reconstruction. Drift correction in the image plane was performed during post-processing, but could, in principle, have been performed live during imaging via feedback to a motorized stage. Re-activation of the Alexa Fluor 647 molecules back from the dark state was performed with 3 W/cm^2 405 nm epi-illumination every hundredth frame after the first 10,000 frames were acquired. Single-molecule data comparing epi-illumination and light sheet illumination is shown in **Supplementary Video 1**.

Acquisition of 3D SR images of microtubules in BS-C-1 cells was performed using a similar scheme as for the lamin B1 sample, with the exception that a 4-µm Tetrapod PSF was used for single-molecule detection and a 6-µm Tetrapod PSF was used for fiducial imaging. No 405 nm re-activation was used in this case. Single-molecule data aqcuired using the 4-µm Tetrapod PSF is shown in **Supplementary Video 2**.

To demonstrate the versatility of the imaging platform, the DM was replaced by a transmissive dielectric phase mask for 3D SR imaging of mitochondria in HeLa cells (**Supplementary Video 5**). In this case, far red fiducial beads were used, allowing for continuous excitation using 647 nm and detection using the DH PSF. Since the range of the PSF covered the entire range of the sample, no live drift correction was necessary. This scheme was very easy to implement and required no scripts to control the setup and only a single laser for illumination.

Mitochondria in HeLa cells were imaged with the DH PSF while switching from epi-illumination to light sheet illumination to allow for direct comparison between the signal, background, and localization precision in the two cases (**Supplementary Video 8**).

Acquisition of 3D SR images of lamin B1 in HeLa cells was performed using a similar scheme as for the 2D lamin B1 sample with interleaved illumination and live axial drift correction. However, in this case the 4*f* system was extended to two channels, where single molecules were detected using the DH PSF in the far red channel and the fiducial beads were detected in the red channel using a 6-µm Tetrapod PSF implemented using a transmissive phase mask. Several slices were aqcuired and the focal plane was moved together with the light sheet to sample the entire nuclear lamina. The positions of the fiducial beads, which were detectable in all slices owing to the long axial range of the Tetrapod PSF, were used to stitch together the different slices during post-processing. The final z-position of each slice was corrected using cross-correlation between two adjacent slices.

Analysis of 2D data. 2D single-molecule localization was performed using the ThunderSTORM[33] plugin in FIJI[34] using wavelet filtering for background subtraction and a weighted least-squares fitting routine. The

bioRxiv preprint doi: https://doi.org/10.1101/135699; this version posted May 9, 2017. The copyright holder for this preprint (which was not certified by peer review) is the author/funder, who has granted bioRxiv a license to display the preprint in perpetuity. It is made available under aCC-BY-NC-ND 4.0 International license.

analysis methodology for extracting the 3D position of the fiducial bead imaged with a 10-µm Tetrapod PSF is described in section **Analysis of Tetrapod data**. The resulting data was filtered to remove localizations with a number of photons per localization higher than 10,000 and localization precision larger than 35 nm. This resulted in ~600,000 localizations with a median of 2,530 photons per localization, 28 background photons per pixel, and a 2D localization precision of 19 nm (**Supplementary Fig. 5b**). The localizations were reconstructed as 2D histograms in MATLAB using 16x16 nm^2 bins (**Supplementary Fig. 5a**). Gaussian fitting of a line scan over the localizations resulted in a measured nuclear lamina width of 130 nm (FWHM).

Analysis of Tetrapod data. Localization analysis of Tetrapod PSF data was performed using an imaging model based on the Gibson-Lanni scalar diffraction approximation for mismatched refractive indices[35]. In the model used here, the PSF was calculated from the pupil plane electric field. For an on-axis point source located at the coverslip surface and coincident with the focal plane of the objective, this field is given by

$$P(\rho,\varphi)=\frac{\mathrm{circ}(\rho)}{\left[1-\left(\frac{NA}{n_1}\rho\right)^2\right]^{1/4}}\exp\left[i\mathfrak{M}(\rho,\varphi)\right] \tag{8}$$

where $\rho\in(0,1]$ is the normalized radial coordinate of the pupil plane, φ is the azimuthal coordinate, NA is the numerical aperture, n_1 is the refractive index of the immersion medium, and $\mathfrak{M}(\rho,\varphi)$ is the particular Tetrapod phase pattern. The circle function limits the field to spatial frequencies in the passband of the objective, while the denominator accounts for compression of the spherical wavefront onto the pupil plane[36].

In a sample with a planar index mismatch created by the boundary between the coverslip/immersion medium (n_1=1.518) and sample ($n_2\approx1.33$), the axial position of a fluorophore is determined by two parameters: (1) its distance from the coverslip, z_{em}, and (2) the distance of the nominal focal plane of the objective from the coverslip, f_{nom}, corresponding to physical translation of the objective from perfect focus at the coverslip surface. Each parameter is associated with a corresponding phase term based on the accumulated phase lag of a ray of each spatial frequency in the pupil plane. The overall phase contributed by the two parameters is given by

$$\Psi_{depth}(\rho,\varphi\,|\,z_{em},f_{nom})=\frac{2\pi}{\lambda}\left[n_2 z_{em}\sqrt{1-\left(\frac{NA}{n_2}\rho\right)^2}-n_1 f_{nom}\sqrt{1-\left(\frac{NA}{n_1}\rho\right)^2}\right]. \tag{9}$$

Inclusion of this depth factor produced qualitatively similar PSFs to those observed in experiment. However, the presence of slight optical aberrations in the setup led to reduced precision and accuracy in some regions of the axial range due to disagreement between the model and experimental PSFs[37]. In order to account for these aberrations, a new phase retrieval algorithm[37] was used to determine a single additional phase factor, $\Psi_{aberr}(\rho,\varphi)$ appropriate for the entire *z*-range, which yielded a final pupil plane electric field given by

$$P_{aberr}(\rho,\varphi)=P(\rho,\varphi)\exp\left\{i\left[\Psi_{depth}(\rho,\varphi\,|\,z_{em},f_{nom})+\Psi_{aberr}(\rho,\varphi)\right]\right\}. \tag{10}$$

Phase retrieval was performed using calibration images of fiducial beads present in the samples, and separate calculations of Ψ_{aberr} were made for each sample and each PSF. A final but important

bioRxiv preprint doi: https://doi.org/10.1101/135699; this version posted May 9, 2017. The copyright holder for this preprint (which was not certified by peer review) is the author/funder, who has granted bioRxiv a license to display the preprint in perpetuity. It is made available under aCC-BY-NC-ND 4.0 International license.

consideration was the calibration of slight localization biases in both the lateral and axial directions, which arise due to the low symmetry of certain aberrations[38] and small outstanding differences between the model and experimental PSFs. These biases were calibrated by localizing images from a scan of the fiducial bead over the axial range of the Tetrapod PSF, in which the lateral position remained constant and the axial position was known. The bias, or offset between the estimated and known positions, was calculated in each dimension as a function of the axial position of the objective. Each single-molecule localization was then corrected for biases in 3D using a polynomial interpolation of the bias evaluated at the estimated axial position.

Super-resolution image data was treated with a 200-frame temporal quantile filter to reduce background inhomogeneities prior to fitting. Single-molecule Tetrapod PSFs were detected via phase correlation using a library of calculated model PSFs which sampled the relevant axial range in 100 nm increments. A maximum-likelihood estimation routine was used to finely determine the 3D position of the emitter, signal photons in the PSF, and background photons remaining after the quantile filtering. In each frame, the nominal focus of the objective was determined by interpolation of drift data extracted from localizations of the fiducial bead (which had a known, constant *z* position). Localization biases and 3D sample drift were compensated to produce final data sets.

The data used for reconstructing the microtubule image was filtered to remove localizations with a number of photons per localization lower than 1,000 and higher than 30,000, background photons per pixel lower than 9 and higher than 30, and with an objective function value larger than -4,000. This resulted in ~40,000 localizations with a median of 8,800 photons per localization and 17 background photons per pixel (**Supplementary Fig. 8**). The background value reported here is calculated after subtraction of the temporal background filter. Repetitive localization of isolated, stationary molecules resulted in an estimated average localization precision of 10 nm in xy and 15 nm in z. Here histograms of the single-molecule localizations in x, y, and z were fit to 1D Gaussians and the localization precision was estimated from the standard deviations of the fits. The localizations were rendered using the Vutara SRX software from Bruker, where spurious localizations were removed by means of filtering for large average distance to eight nearest neighbors (**Fig. 2b** and **Supplementary Video 3**).

To estimate the localization precision of the axially highest fiducial fluorescent bead used for reconstructing the 3D lamin image using the 6-µm Tetrapod PSF in the red channel for detection, the x, y, and z positions were low-pass filtered and the resulting low-pass filtered traces were subtracted from the x, y, and z localizations before analysis. The histograms of the resulting x, y, and z localizations were fit with 1D Gaussians and the localization precision in x, y, and z was estimated from the standard deviations of the fits. This resulted in an estimated average localization precision of 3 nm in xy and 7 nm in z (**Supplementary Fig. 12b**).

Analysis of double-helix data. Calibration and fitting analysis of DH PSF images were performed using a modified version of the open-source Easy-DHPSF software[39] (https://sourceforge.net/projects/easy-dhpsf/). When analyzing images of the DH PSF, the lobes of each PSF were fitted using non-linear least-squares functions in MATLAB with a pair of identical, radially symmetric 2D Gaussians as the objective function. The localization precision was calculated using the calibration described in Ref.[40]. The agreement of this calibration with the achievable localization precision in our new imaging platform was verified by imaging and localizing isolated, stationary molecules on a coverslip for typical signal and background photon numbers.

bioRxiv preprint doi: https://doi.org/10.1101/135699; this version posted May 9, 2017. The copyright holder for this preprint (which was not certified by peer review) is the author/funder, who has granted bioRxiv a license to display the preprint in perpetuity. It is made available under aCC-BY-NC-ND 4.0 International license.

The data used for reconstructing the mitochondria images was filtered to remove localizations with a number of photons per localization higher than 20,000, distance between lobes smaller than 6 pixels and larger than 7.5 pixels, and z localization precision larger than 50 nm. This resulted in ~240,000 localizations with a median of 4,857 photons per localization, 46 background photons per pixel, and localization precisions of 13 nm and 20 nm in xy and z respectively (**Supplementary Fig. 9b**). The localizations were rendered using the Vutara SRX software from Bruker (**Fig. 2b, c**, **Supplementary Fig. 9a**, and **Supplementary Videos 6** and **7**).

Single-molecule data acquired with the DH PSF comparing epi-illumination (Epi) and light sheet (LS) illumination were analyzed in the same manner as the data used for the 3D SR mitochondria reconstruction. The data was filtered to remove localizations with a distance between lobes smaller than 6 pixels and larger than 7.5 pixels. Using Epi/LS resulted in 413/1,061 localizations with a median of 3,181/3,857 photons per localization, 103/46 background photons per pixel, and localization precision of 23/16 nm and 35/24 nm in xy and z, respectively, demonstrating the drastic improvement in localization precision when using light sheet illumination (**Supplementary Fig. 10** and **Supplementary Video 8**).

The data used for reconstructing the 3D lamin B1 image was filtered to remove localizations with a distance between lobes smaller than 5.5 pixels and larger than 10 pixels, and background photons per pixel larger than 200. This resulted in ~525,000 localizations with a median of 8,465 ± 791 photons per localization and 50 ± 9 background photons per pixel (**Supplementary Fig. 11**). The values are given as mean ± standard deviation of the median values in each z-slice. The median z position of the localizations in each slice was 1.1 µm, 1.7 µm, 2.9 µm, 3.7 µm, 4.7 µm, and 4.7 µm for slices 1-6, respectively. The localizations were rendered using the Vutara SRX software from Bruker, where spurious localizations were removed by means of filtering for large average distance to eight nearest neighbors (**Fig. 2d** and **Supplementary Videos 10-12**). The localization precision 3.3 µm above the coverslip was estimated from repetitive localization of an isolated, stationary, green fiducial bead with some spectral bleed-through into the single-molecule far red channel. This dim bead yielded a median of 1,467 photons per localization and 29 background photons per pixel (**Supplementary Fig. 12a**). Using the equations for localization precision of the DH PSF derived by Rieger *et al.*[41] and inserting typical PSF parameters and the median signal and background values of the bead and SM localizations, it was found that the localization precision of the bead should be worse than that for a typical single molecule. An estimation using the localizations from the bead should thus result in a conservative measure of the localization precision. Histograms of the bead localizations in x, y, and z were fit to 1D Gaussians and the localization precision was estimated from the standard deviations of the fits. This resulted in an estimated average localization precision of 16 nm in xy and 23 nm in z. The thickness of the lamina at the bottom and at the top of the nucleus was estimated by fitting the localizations in z of small xy-regions at the bottom and top of the nucleus, respectively, to 1D Gaussians and calculating the FWHM of the fits. This resulted in estimated thicknesses of 113 nm and 101 nm for the bottom and top, respectively (**Supplementary Fig. 12c**).

Code availability. The custom-written code generated during the current study is available from the corresponding author upon request.

Data availability. The single-molecule localizations generated and analyzed during the current study are available from the corresponding author upon request.

bioRxiv preprint doi: https://doi.org/10.1101/135699; this version posted May 9, 2017. The copyright holder for this preprint (which was not certified by peer review) is the author/funder, who has granted bioRxiv a license to display the preprint in perpetuity. It is made available under aCC-BY-NC-ND 4.0 International license.

24. Backlund, M. P. *et al*. *Proc. Natl. Acad. Sci. U. S. A.* **109**, 19087-19092 (2012).
25. Corle, T. R. & Kino, G. S, Academic Press (1996).
26. Ram, S., Prabhat, P., Ward, E. S. & Ober, R. J. *Opt. Express* **17**, 6881-6898 (2009).
27. Juette, M. F. *et al*. *Nat. Methods* **5**, 527-529 (2008).
28. Hajj, B. *et al*. *Proc. Natl. Acad. Sci. U. S. A.* **111**, 17480-17485 (2014).
29. Huang, F. *et al*. *Cell* **166**, 1028-1040 (2016).
30. Shtengel, G. *et al*. *Proc. Natl. Acad. Sci. U. S. A.* **106**, 3125-3130 (2009).
31. Lew, M. D., Lee, S. F., Badieirostami, M. & Moerner, W. E. *Opt. Lett.* **36**, 202-204 (2011).
32. Halpern, A. R., Howard, M. D. & Vaughan, J. C. *Curr Protoc Chem Biol*, 103-120 (2015).
33. Ovesny, M., Krizek, P., Borkovec, J., Svindrych, Z. & Hagen, G. M. *Bioinformatics* **30**, 2389-2390 (2014).
34. Schindelin, J. *et al*. *Nature methods* **9**, 676-682 (2012).
35. Gibson, S. F. & Lanni, F. *J. Opt. Soc. Am. A* **8**, 1601-1613 (1991).
36. Richards, B. & Wolf, E. *Proc. R. Soc. London Ser. A* **253**, 358-379 (1959).
37. Petrov, P. N., Shechtman, Y. & Moerner, W. E. *Opt. Express* **25**, 7945-7959 (2017).
38. Carlini, L., Holden, S. J., Douglass, K. M. & Manley, S. *Plos One* **10**, e0142949 (2015).
39. Lew, M. D., von Diezmann, A. R. S. & Moerner, W. E. *Protocol Exchange*, 026 (2013).
40. Gahlmann, A. *et al*. *Nano Lett.* **13**, 987-993 (2013).
41. Rieger, B. & Stallinga, S. *ChemPhysChem* **15**, 664-670 (2014).

bioRxiv preprint doi: https://doi.org/10.1101/135699; this version posted May 9, 2017. The copyright holder for this preprint (which was not certified by peer review) is the author/funder, who has granted bioRxiv a license to display the preprint in perpetuity. It is made available under aCC-BY-NC-ND 4.0 International license.

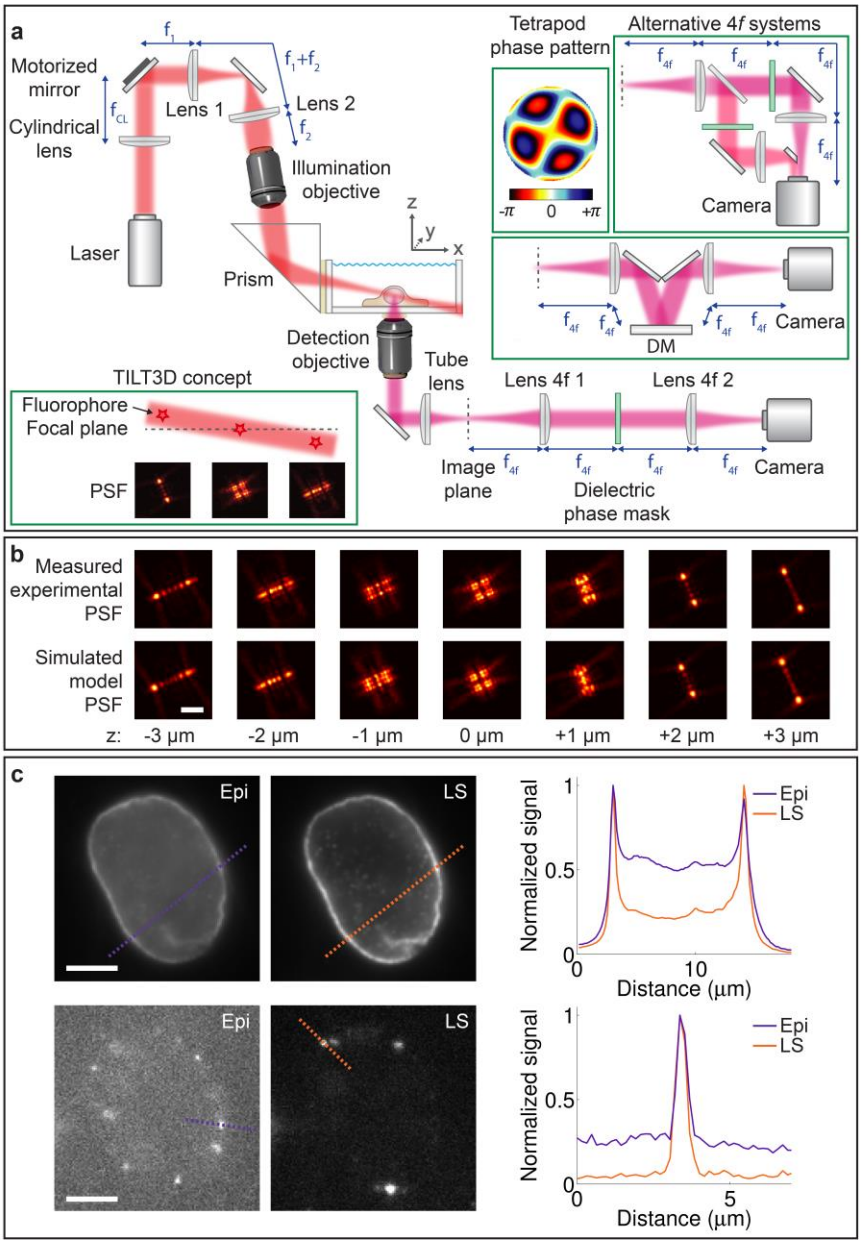

Figure 1 Design and performance of TILT3D. **(a)** Simplified schematic of the setup. The light sheet is formed by a cylindrical lens, relayed to the back aperture of a long-working distance illumination objective, and reflected at an angle into the sample using a glass prism. A motorized mirror is used to adjust the y- and z-position of the light sheet. The emitted light is imaged through a 4*f* system where a transmissive dielectric phase mask or a deformable mirror (DM) is placed in the Fourier plane for phase modulation. The phase pattern reshapes the point spread function (PSF) to encode the axial position of the emitter over several microns. Upper left inset shows the phase pattern for a Tetrapod PSF with 6 µm axial range. Upper right insets show the 4*f* systems when using a DM in the Fourier plane and when using two channels with transmissive phase masks. Lower left inset shows the concept of TILT3D, where the light sheet is tilted and fluorophore positions are detected using long axial range PSFs. **(b)** Images showing the experimentally measured (top) and computationally modeled (bottom) PSF of a single emitter using the

bioRxiv preprint doi: https://doi.org/10.1101/135699; this version posted May 9, 2017. The copyright holder for this preprint (which was not certified by peer review) is the author/funder, who has granted bioRxiv a license to display the preprint in perpetuity. It is made available under aCC-BY-NC-ND 4.0 International license.

6-µm Tetrapod phase pattern shown in **a**. Scale bar is 3 µm. **(c)** Diffraction-limited (top) and single-molecule (bottom) images of lamin B1 immunolabeled with Alexa Fluor 647 in a HeLa cell demonstrating that light sheet illumination (LS) improves the signal-to-background ratio up to five-fold compared to conventional epi-illumination (Epi). Graphs show line scans over the dashed lines in the images. Diffraction-limited images and single-molecule images are shown with the same linear grayscale, respectively. Scale bars are 5 µm.

bioRxiv preprint doi: https://doi.org/10.1101/135699; this version posted May 9, 2017. The copyright holder for this preprint (which was not certified by peer review) is the author/funder, who has granted bioRxiv a license to display the preprint in perpetuity. It is made available under aCC-BY-NC-ND 4.0 International license.

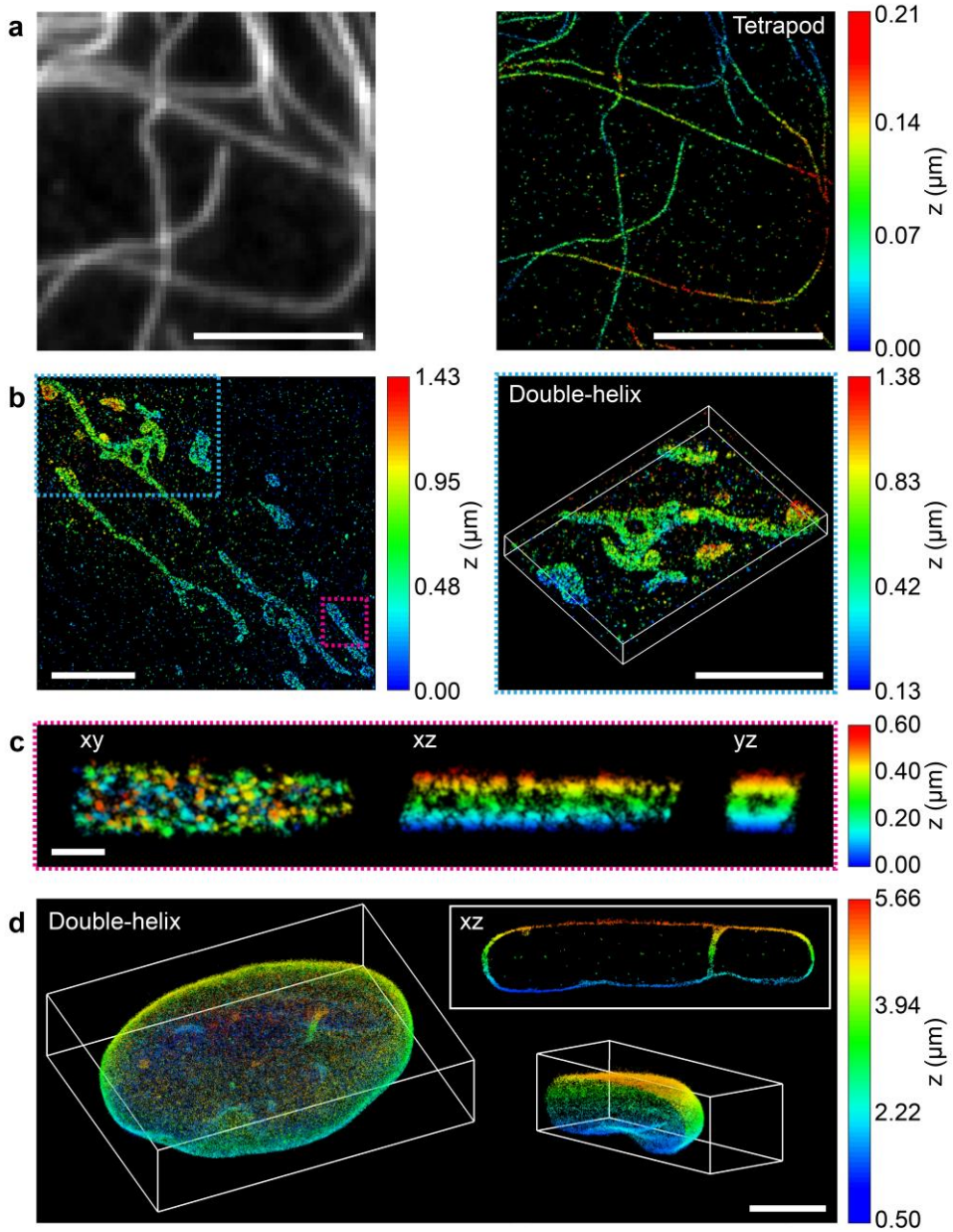

Figure 2 Tilted light sheet imaging with long axial range PSFs. **(a)** Diffraction limited image and 3D super-resolution (SR) reconstruction of microtubules (α/β-tubulin) in a BS-C-1 cell. Imaging of single molecules and fiducial beads was performed with 4-µm and 6-µm Tetrapod PSFs, respectively. **(b)** 3D SR reconstructions of mitochondria (TOM20) in a HeLa cell. Imaging of single molecules and fiducial beads was performed with the double-helix (DH) PSF. **(c)** xy, xz, and yz views of the mitochondrion shown in the magenta rectangle in **c**, revealing the hollow cylinder structure of the mitochondrial outer membrane. **(d)** 3D SR reconstruction of the entire nuclear lamina (lamin B1) in a HeLa cell. Imaging of single molecules and fiducial beads was performed with the DH PSF and a 6-µm Tetrapod PSF, respectively. The xz view shows a 1.3-µm thick y-slice through the cell, where lamin meshwork enveloping an intranuclear channel is visible. The lower right inset shows the right cap of the reconstruction. All samples imaged were immunolabeled with Alexa Fluor 647. Scale bars are 5 µm in **a**, **b**, and **d**, and 500 nm in **c**.

bioRxiv preprint doi: https://doi.org/10.1101/135699; this version posted May 9, 2017. The copyright holder for this preprint (which was not certified by peer review) is the author/funder, who has granted bioRxiv a license to display the preprint in perpetuity. It is made available under aCC-BY-NC-ND 4.0 International license.

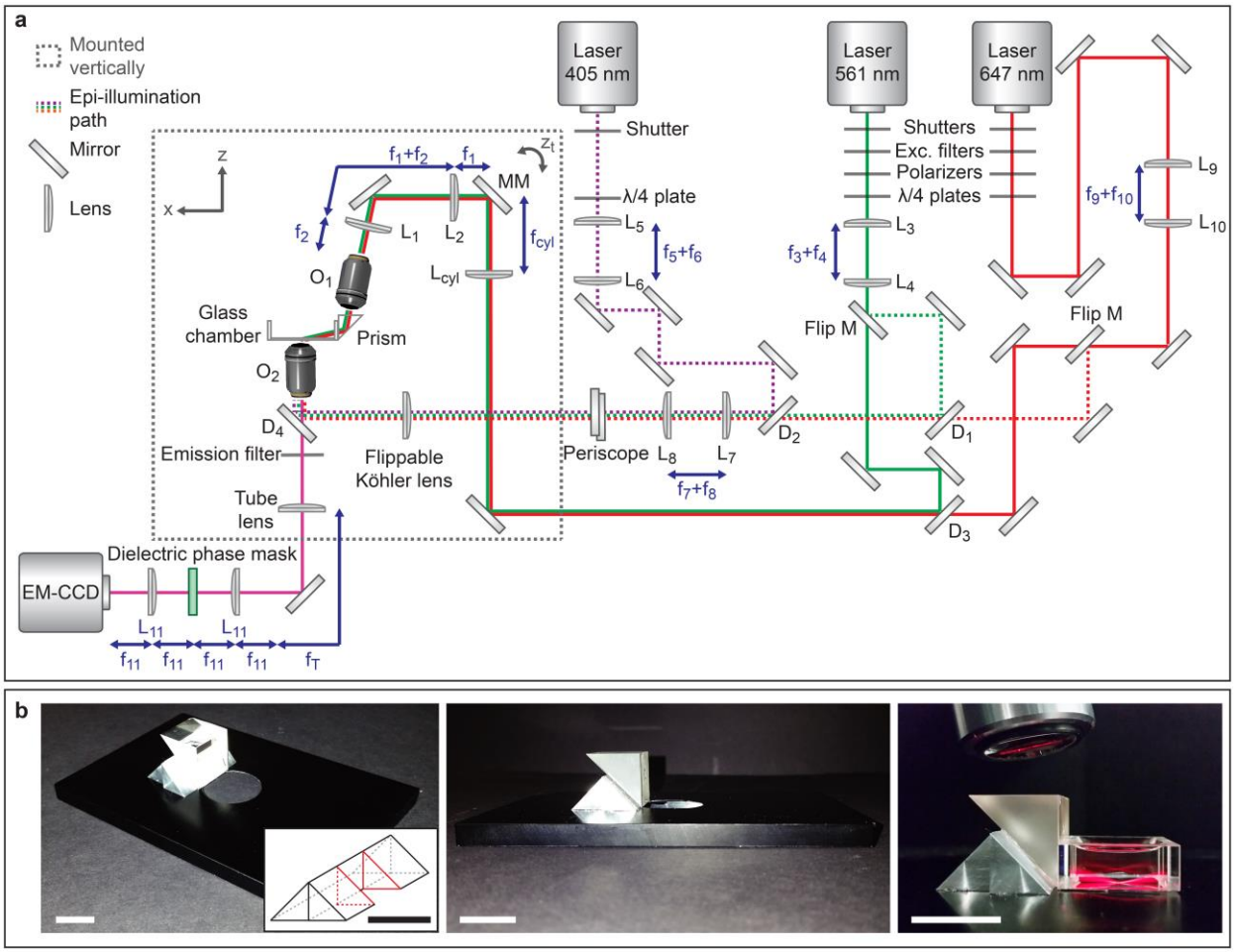

Supplementary Figure 1 Illustrations of the imaging platform. **(a)** Detailed schematic of the optical setup shown for a single-channel 4*f* setup with a transmissive dielectric phase mask. Tilting the motorized mirror (MM) in the direction given by the gray, semicircular arrow, z_t, indicates translation of the light sheet in z. Translation in y is performed by tilting the mirror in the perpendicular direction. L_1-L_{11}: lenses, f_1-f_{11}: focal lengths of lenses, Flip M: flip mirror, D_1-D_4: dichroic mirrors, L_{cyl}: cylindrical lens, f_{cyl}: focal length of cylindrical lens, O_1: illumination objective, O_2: detection objective. **(b)** Photos of the glass prism attachment on the microscope stage. The glass prism is attached to a right triangular aluminum prism with a hole cut out of the back to create an air-glass interface for total internal reflection to occur (inset schematic shows the Al support). The rightmost photo shows the light sheet being reflected by the prism into a fluorescent solution (1:1000 Alexa Fluor 647 conjugated secondary antibodies (Abcam, ab150067) in water) in the sample chamber. Scale bars are 2 cm.

bioRxiv preprint doi: https://doi.org/10.1101/135699; this version posted May 9, 2017. The copyright holder for this preprint (which was not certified by peer review) is the author/funder, who has granted bioRxiv a license to display the preprint in perpetuity. It is made available under aCC-BY-NC-ND 4.0 International license.

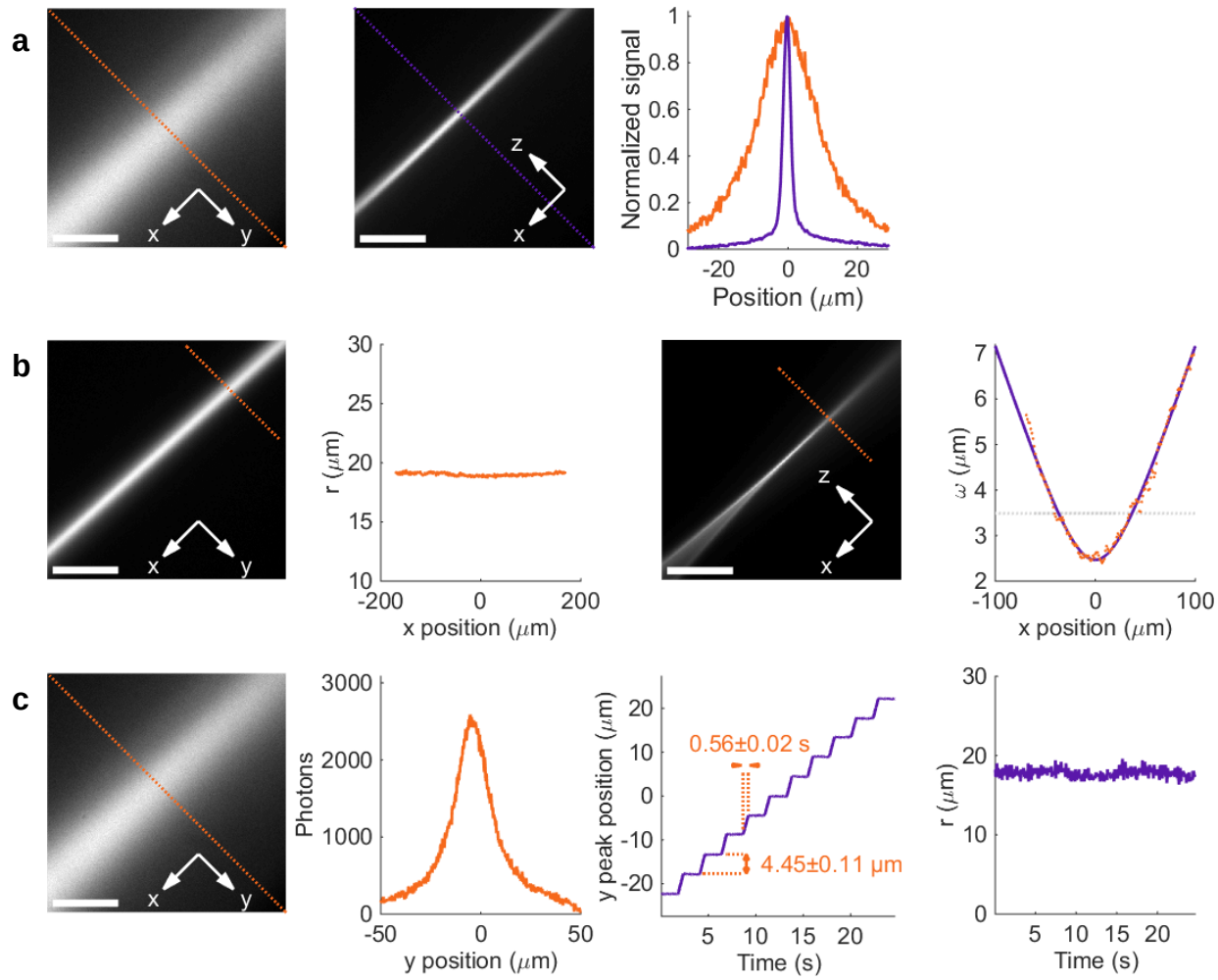

Supplementary Figure 2 Light sheet characteristics. **(a)** Images showing the width and thickness of the light sheet. The graph shows line scans along y and z for estimation of width and thickness, respectively, using the axis definitions in **Figure 1a**. Fitting 1D Gaussians to the line scans allowed estimation of the thickness and width to be 2.1 µm and 18.7 µm ($1/e^2$), respectively. **(b)** To estimate the width variation (left) and the confocal parameter (right) along the direction of beam propagation, x, the light sheet was imaged using a 20x objective. The light sheet profiles were determined by measuring the cross-sectional intensity along different parts of the light sheet in y and z (orange dots in graphs on right). Fitting 1D Gaussians to the line scans, the width of the light sheet was measured to be 19.1 ± 0.1 µm over a range of 340 µm in the direction of beam propagation, demonstrating that the width remains relatively constant across the entire field of view. The thickness dependence was well described using the Gaussian beam propagation equation (purple line), resulting in an experimental confocal parameter of 73.4 µm for a beam of thickness 2.5 µm ($1/e^2$). **(c)** To estimate the relationship between the step size of the motorized mirror and the translation of the light sheet along y in the sample plane the mirror was scanned in 1000 steps intervals (left). The cross-sectional profile of the light sheet was measured by intensity line scanning of the resulting images in y (mid left), and 1D Gaussian fitting of the line scans was used to estimate the center position of the light sheet as a function of time throughout the scanning of the motorized mirror (mid right). Calculating the mean position at each scan step resulted in a translation of 4.45 ± 0.11 µm per

bioRxiv preprint doi: https://doi.org/10.1101/135699; this version posted May 9, 2017. The copyright holder for this preprint (which was not certified by peer review) is the author/funder, who has granted bioRxiv a license to display the preprint in perpetuity. It is made available under aCC-BY-NC-ND 4.0 International license.

1000 steps, corresponding to a single step translation of about 4.5 nm. The time to complete the translation of 1000 steps was estimated to be 0.56 ± 0.02 s. During a total scan distance of 45 µm, the width of the light sheet was measured to 17.8 ± 0.6 µm ($1/e^2$), showing that the width remains relatively constant across the scan range (right). In all measurements the light sheet profiles were imaged in a fluorescent solution (1:1000 Alexa Fluor 647 conjugated secondary antibodies (Abcam, ab150067) in water). The thickness (z) was imaged by rotating the cylindrical lens by 90°. Scale bars are 20 µm in **a** and **c**, and 100 µm in **b**.

bioRxiv preprint doi: https://doi.org/10.1101/135699; this version posted May 9, 2017. The copyright holder for this preprint (which was not certified by peer review) is the author/funder, who has granted bioRxiv a license to display the preprint in perpetuity. It is made available under aCC-BY-NC-ND 4.0 International license.

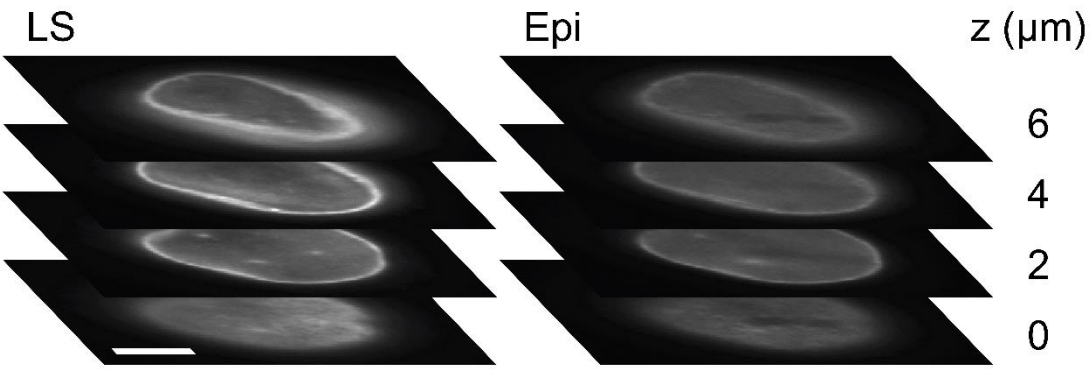

Supplementary Figure 3 Sectioning using the tilted light sheet. Image stacks showing lamin B1 in a HeLa cell immunolabeled with Alexa Fluor 647 imaged using either light sheet (LS) illumination or epi-illumination (Epi). The image plane was moved using the piezoelectric objective scanner, and for LS imaging the LS plane was moved together with the image plane using the motorized mirror. The sectioning capability of the LS is clearly demonstrated, showing an improved contrast when compared with epi-illumination for all cell sections. Images are shown with the same linear grayscale. Scale bar is 5 µm.

bioRxiv preprint doi: https://doi.org/10.1101/135699; this version posted May 9, 2017. The copyright holder for this preprint (which was not certified by peer review) is the author/funder, who has granted bioRxiv a license to display the preprint in perpetuity. It is made available under aCC-BY-NC-ND 4.0 International license.

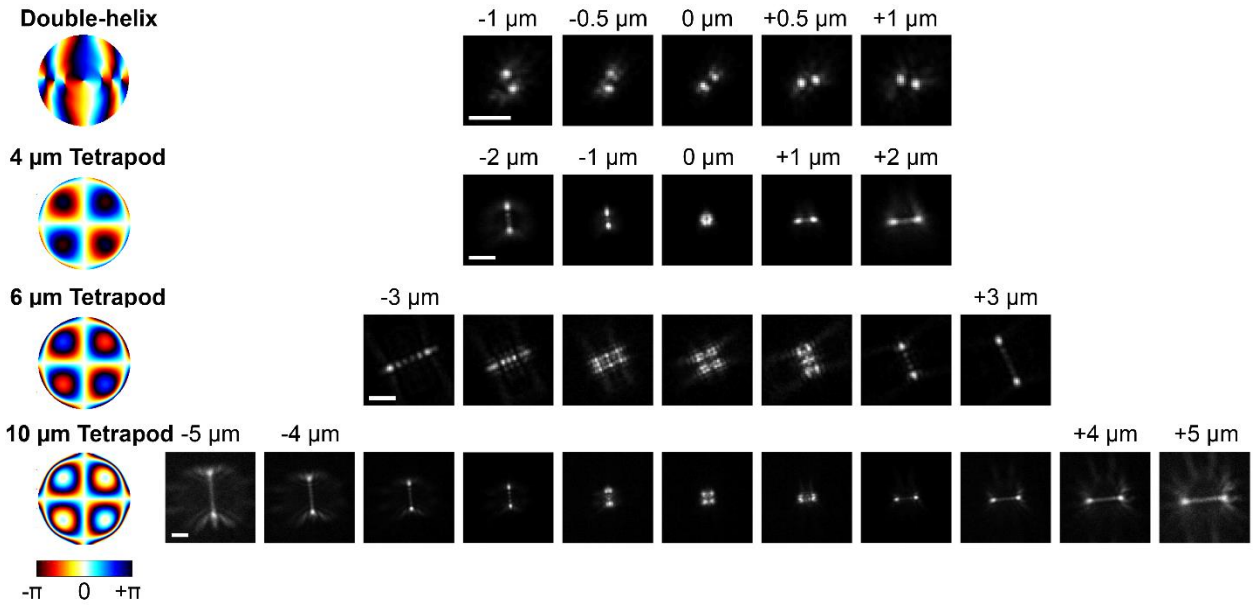

Supplementary Figure 4 Phase patterns and experimental point spread functions (PSFs). Theoretical phase patterns used to generate the double-helix (DH) PSF, which has an axial range of ~2-3 µm, and Tetrapod PSFs with axial ranges of 4 µm, 6 µm, and 10 µm. The DH and the 6-µm Tetrapod phase patterns were implemented using a transmissive dielectric phase mask, while the patterns for the 4-µm and 10-µm Tetrapod PSFs were implemented using a deformable mirror. PSF images show a fluorescent bead on a cover slip imaged using the different phase masks while scanning the nominal focus to the positions indicated above the images. Scale bars are 3 µm.

bioRxiv preprint doi: https://doi.org/10.1101/135699; this version posted May 9, 2017. The copyright holder for this preprint (which was not certified by peer review) is the author/funder, who has granted bioRxiv a license to display the preprint in perpetuity. It is made available under aCC-BY-NC-ND 4.0 International license.

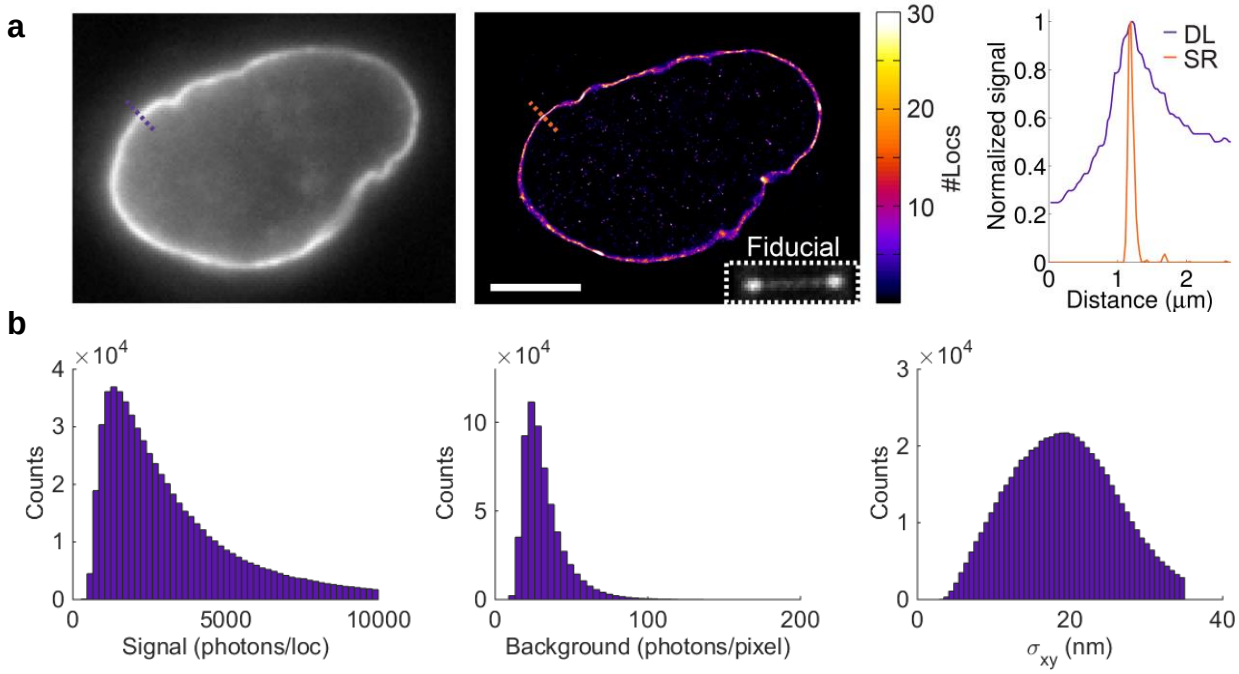

Supplementary Figure 5 2D imaging of nuclear lamina. **(a)** Diffraction-limited (DL) image and 2D super-resolution (SR) reconstruction of the nuclear lamina (lamin B1) in a HeLa cell. Inset shows the fiducial bead imaged with a 10-µm Tetrapod PSF used for real-time axial drift correction. The graph shows line scans at the corresponding dotted lines in the figures. By fitting the SR line scan with a 1D Gaussian function, the thickness of the nuclear lamina (FWHM) was determined to be 130 nm in the SR reconstruction. Scale bar is 5 µm. **(b)** Histograms showing the signal photons per localization, background photons per pixel, and xy localization precision of the data shown in **a** acquired using the standard point spread function. The data was filtered to remove localizations with a number of photons per localization higher than 10,000 and localization precision larger than 35 nm. This resulted in ~600,000 filtered localizations with median photons per localization of 2,530, background photons per pixel of 28, and localization precision of 19 nm.

bioRxiv preprint doi: https://doi.org/10.1101/135699; this version posted May 9, 2017. The copyright holder for this preprint (which was not certified by peer review) is the author/funder, who has granted bioRxiv a license to display the preprint in perpetuity. It is made available under aCC-BY-NC-ND 4.0 International license.

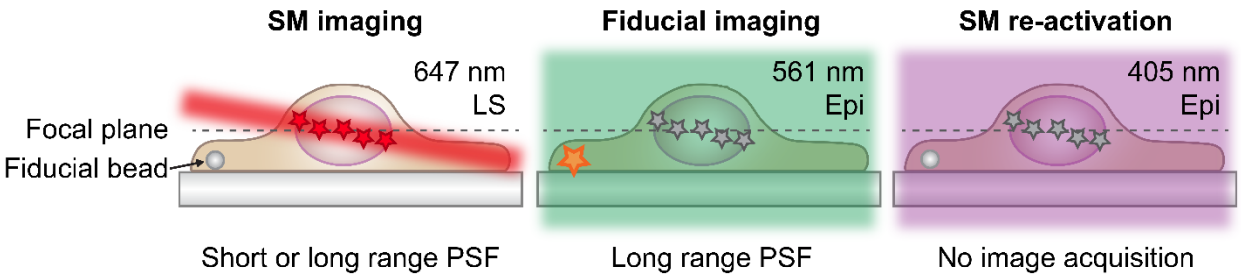

Supplementary Figure 6 Schematic of interleaved illumination and detection scheme (not to scale). Single-molecules (SM) were excited using light sheet (LS) illumination and detected using either a short or long axial range PSF. SM imaging was interleaved with imaging of a fiducial bead that could be positioned anywhere in the field of view. The fiducial bead was excited using epi-illumination (Epi) and detected using a long axial range PSF to allow illumination and detection independent of the axial position of the bead. Using different excitation wavelengths for the sample and the fiducial bead prevented saturation of the camera pixels by the PSF of the bead during SM imaging, while keeping a high photon count (i.e. good localization precision) for the fiducial. The fiducial bead was localized in real time and the sample drift was corrected in the axial direction. The illumination was also interleaved with SM re-activation using a 405 nm laser.

bioRxiv preprint doi: https://doi.org/10.1101/135699; this version posted May 9, 2017. The copyright holder for this preprint (which was not certified by peer review) is the author/funder, who has granted bioRxiv a license to display the preprint in perpetuity. It is made available under aCC-BY-NC-ND 4.0 International license.

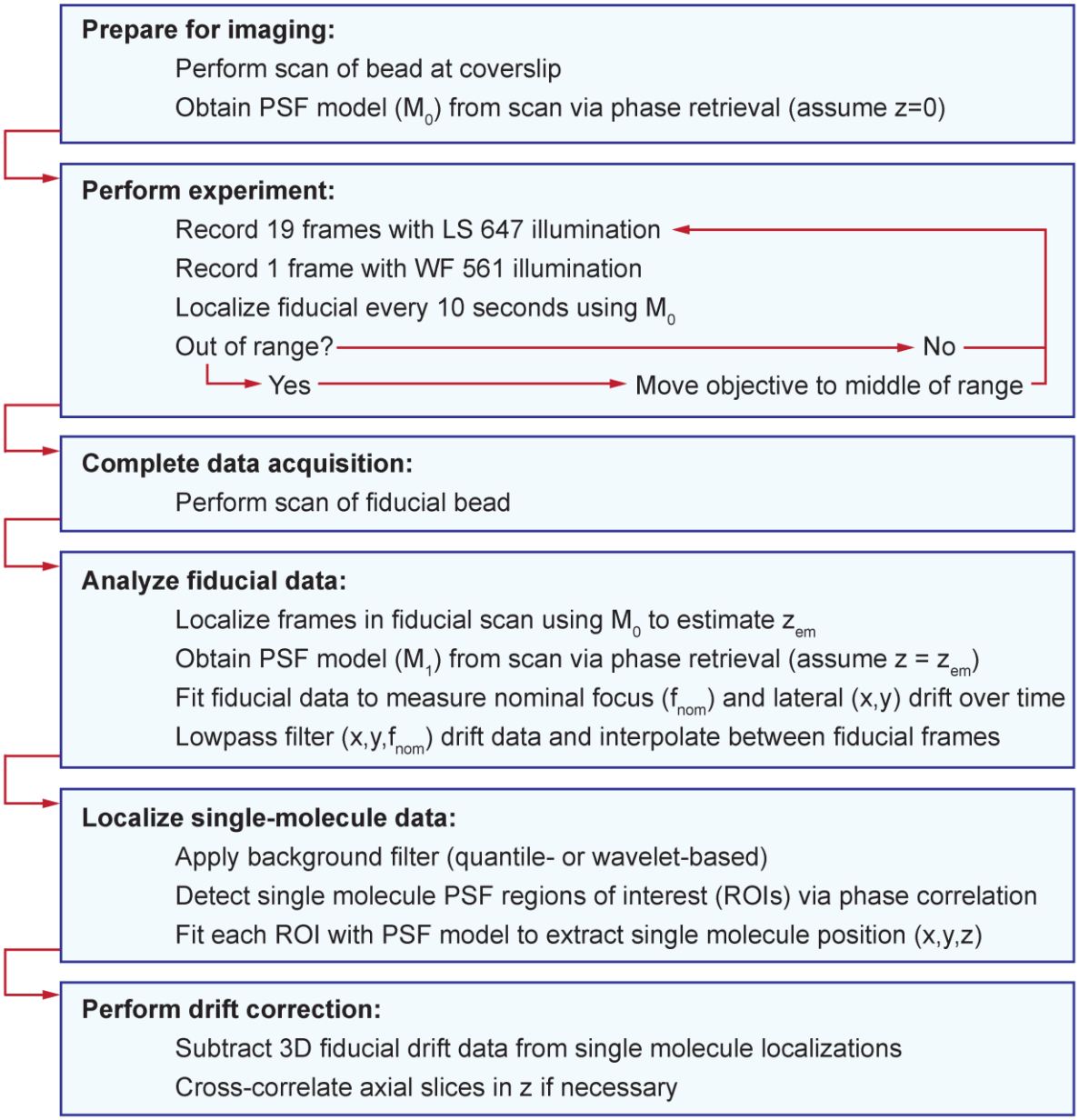

Supplementary Figure 7 Flow chart showing the analysis methodology used for Tetrapod point spread functions. For analysis of fiducial beads only, the **Localize single-molecule data step** can be omitted and performed with separate algorithms available for e.g. the standard PSF or the double-helix PSF.

bioRxiv preprint doi: https://doi.org/10.1101/135699; this version posted May 9, 2017. The copyright holder for this preprint (which was not certified by peer review) is the author/funder, who has granted bioRxiv a license to display the preprint in perpetuity. It is made available under aCC-BY-NC-ND 4.0 International license.

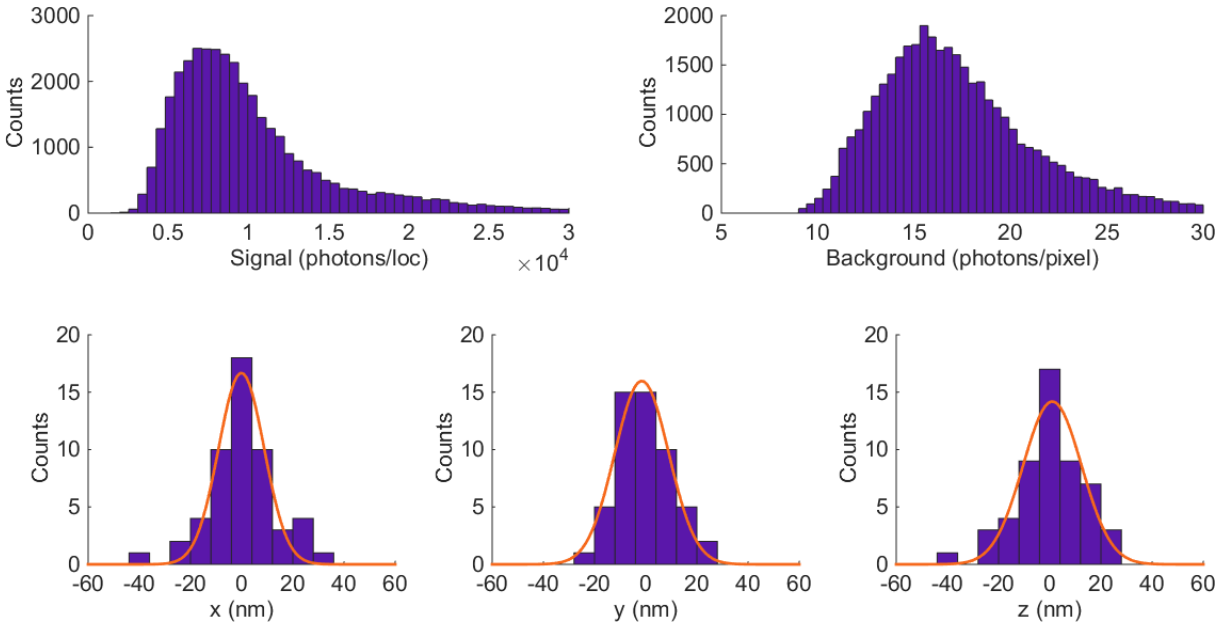

Supplementary Figure 8 Statistics of 4-µm Tetrapod PSF localization data used for microtubule reconstruction. Top row shows histograms of the signal photons per localization and background photons per pixel from the data shown in **Figure 2a**. The data was filtered to remove localizations with a number of photons per localization lower than 1,000 and higher than 30,000, background photons per pixel lower than 9 and higher than 30, and with an objective function value larger than -4,000. This resulted in ~40,000 filtered localizations with median photons per localization of 8,800 and background photons per pixel of 17. Bottom row shows histograms of localizations of an isolated, stationary molecule. The histograms were fit to 1D Gaussians (solid orange lines) and the localization precision in x, y, and z was estimated from the standard deviations of the fits. This resulted in an estimated localization precision for the shown molecule of 10 nm in x and y, and 11 nm in z.

bioRxiv preprint doi: https://doi.org/10.1101/135699; this version posted May 9, 2017. The copyright holder for this preprint (which was not certified by peer review) is the author/funder, who has granted bioRxiv a license to display the preprint in perpetuity. It is made available under aCC-BY-NC-ND 4.0 International license.

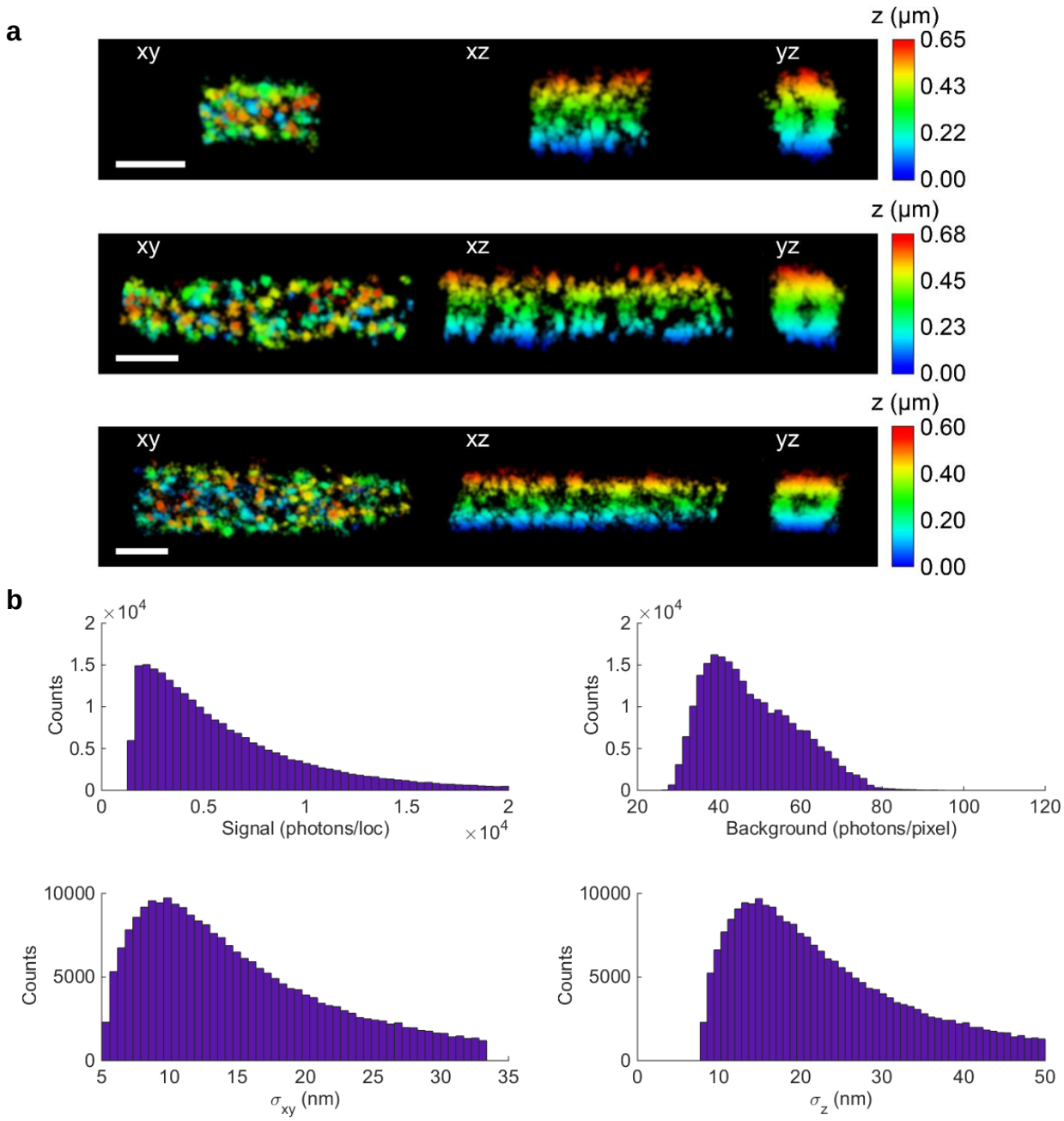

Supplementary Figure 9 Imaging of mitochondrial outer membrane using the double-helix PSF. **(a)** 3D super-resolution reconstructions of three mitochondria (TOM20) in HeLa cells immunolabeled with Alexa Fluor 647, shown in xy, xz, and yz views. Imaging of single molecules and fiducial fluorescent beads was performed using the double-helix PSF. Scale bars are 500 nm. **(b)** Histograms showing the signal photons per localization, background photons per pixel, and xy and z localization precision from the data shown in **Figure 2b** and in **a.** The data was filtered to remove localizations with a number of photons per localization higher than 20,000, distance between lobes smaller than 6 pixels and larger than 7.5 pixels, and z localization precision larger than 50 nm. This resulted in ~240,000 filtered localizations with median photons per localization of 4,857, background photons per pixel of 46, and localization precision of 13 nm and 20 nm in xy and z, respectively.

bioRxiv preprint doi: https://doi.org/10.1101/135699; this version posted May 9, 2017. The copyright holder for this preprint (which was not certified by peer review) is the author/funder, who has granted bioRxiv a license to display the preprint in perpetuity. It is made available under aCC-BY-NC-ND 4.0 International license.

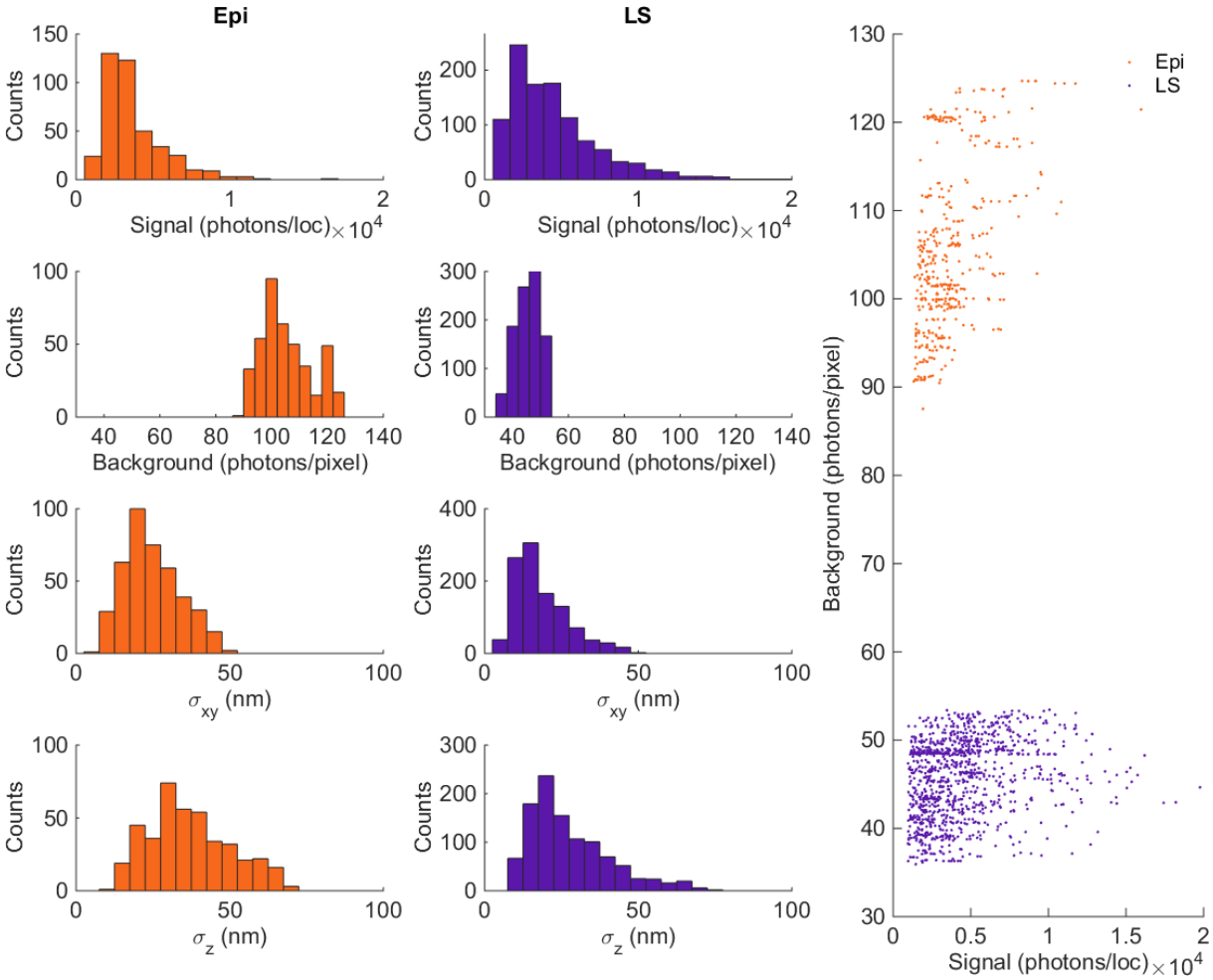

Supplementary Figure 10 Comparison between epi-illumination (Epi) and light sheet (LS) illumination for acquisition of single-molecule data using the double-helix PSF. Histograms showing the signal photons per localization, background photons per pixel, xy and z localization precision, and a direct comparison between the signal and background of localizations in the two cases. Using Epi/LS resulted in 413/1,061 localizations with median photons per localization of 3,181/3,857, background photons per pixel of 103/46, and localization precision of 23/16 nm and 35/24 nm in xy and z, respectively. The sample imaged was mitochondria (TOM20) in HeLa cells immunolabeled with Alexa Fluor 647.

bioRxiv preprint doi: https://doi.org/10.1101/135699; this version posted May 9, 2017. The copyright holder for this preprint (which was not certified by peer review) is the author/funder, who has granted bioRxiv a license to display the preprint in perpetuity. It is made available under aCC-BY-NC-ND 4.0 International license.

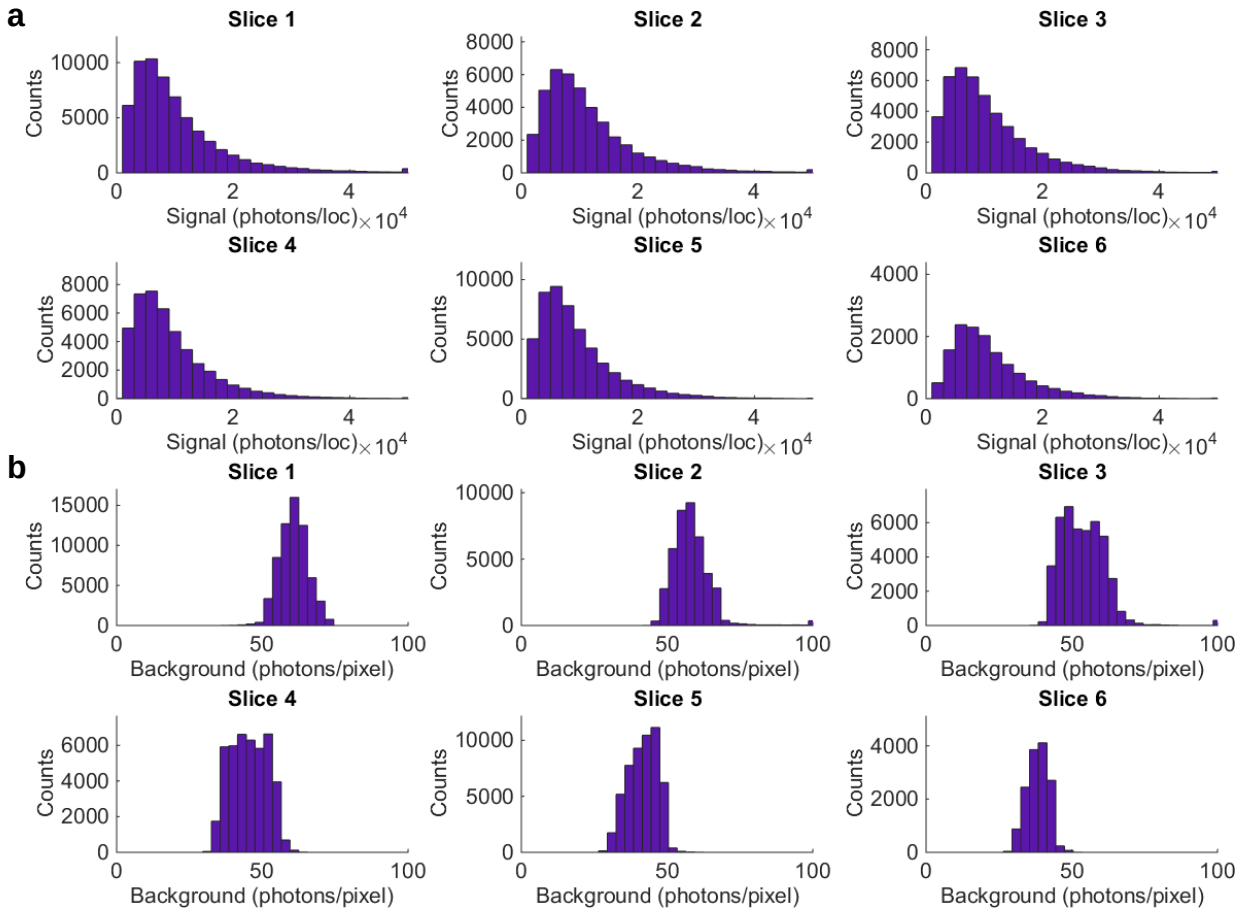

Supplementary Figure 11 Signal and background statistics of double-helix PSF localization data used for the 3D lamin B1 reconstruction. Histograms showing **(a)** signal photons per localization and **(b)** background photons per pixel for six different z-slices used in the reconstruction in **Figure 2d.** The median z position of the localizations in each slice was 1.1 µm, 1.7 µm, 2.9 µm, 3.7 µm, 4.7 µm, and 4.7 µm for slices 1-6, respectively. The data was filtered to remove localizations with a distance between lobes smaller than 5.5 pixels and larger than 10 pixels, and background photons per localization higher than 200. This resulted in ~525,000 localizations with a median of 8,465 ± 791 photons per localization and 50 ± 9 background photons per pixel. The values are given as the mean ± standard deviation of the median values in each z-slice.

bioRxiv preprint doi: https://doi.org/10.1101/135699; this version posted May 9, 2017. The copyright holder for this preprint (which was not certified by peer review) is the author/funder, who has granted bioRxiv a license to display the preprint in perpetuity. It is made available under aCC-BY-NC-ND 4.0 International license.

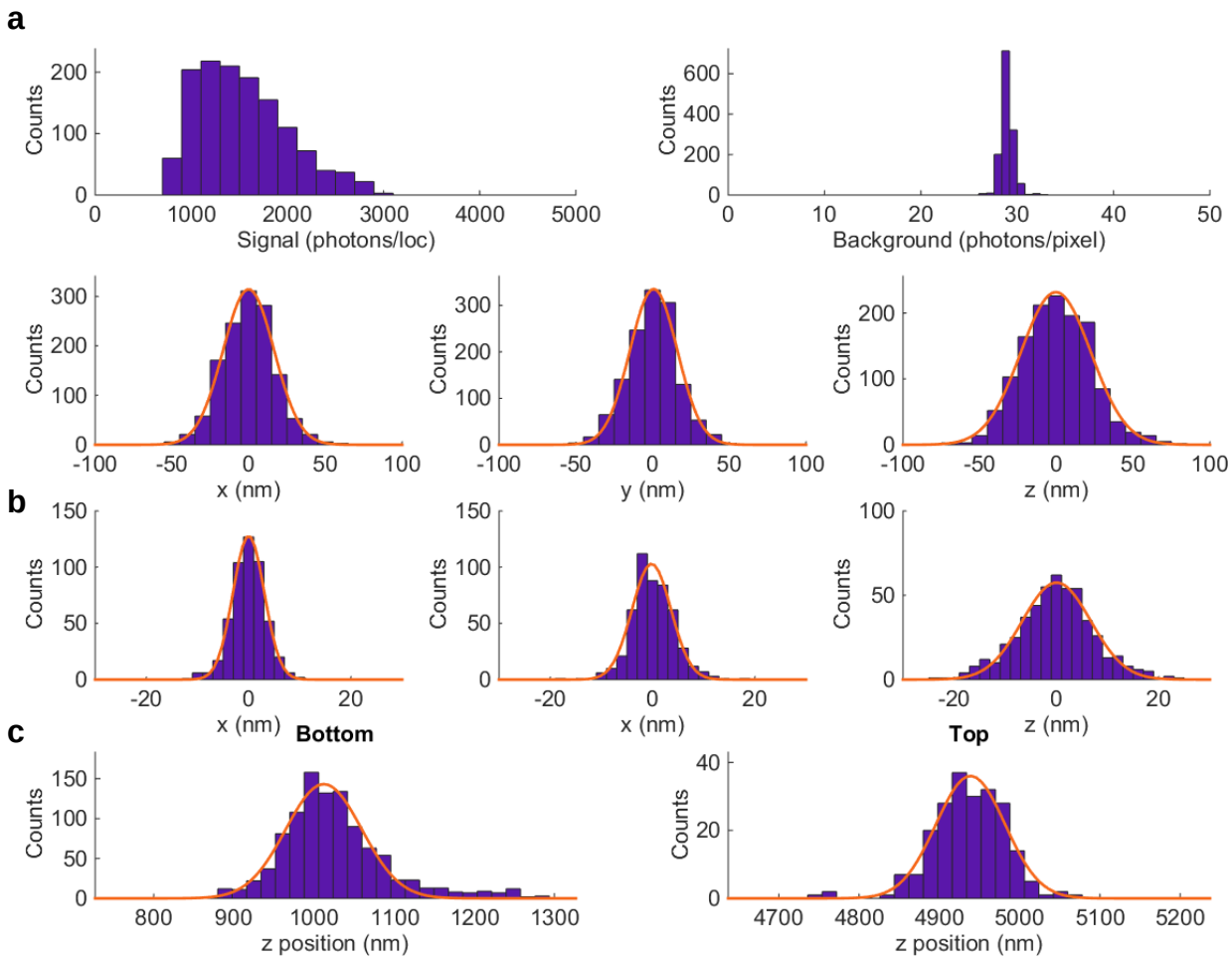

Supplementary Figure 12 Performance of long-axial range PSFs in thick cells. **(a)** Histograms showing the signal photons per localization, background photons per pixel, and x, y, and z positions of localizations of an isolated, stationary bead situated 3.3 µm above the coverslip detected using the double-helix PSF. The bead yielded a median of 1,467 photons per localization and 29 background photons per pixel. The histograms of the x, y, and z localizations were fit to 1D Gaussians (solid orange lines) and the localization precision in x, y, and z was estimated from the standard deviations of the fits. This resulted in an estimated average localization precision of 16 nm in xy and 23 nm in z. **(b)** Histograms showing the x, y, and z positions of the same isolated, stationary bead as in **a** detected using a 6-µm Tetrapod PSF in the second channel (the fiducial bead). Low-pass filtered data of this trace was subtracted before analysis. The histograms of the x, y, and z localizations were fit to 1D Gaussians (solid orange lines) and the localization precision in x, y, and z was estimated from the standard deviations of the fits. This resulted in an estimated average localization precision of 3 nm in xy and 7 nm in z. **(c)** Estimation of measured lamina thickness at the bottom and top of the nucleus. The thickness of the lamina at the bottom and at the top of the nucleus was estimated by fitting the localizations in z of small xy-regions at the bottom and top of the nucleus, respectively, to 1D Gaussians and calculating the FWHM of the fits. This resulted in estimated thicknesses of 113 nm and 101 nm for the bottom and top, respectively.

bioRxiv preprint doi: https://doi.org/10.1101/135699; this version posted May 9, 2017. The copyright holder for this preprint (which was not certified by peer review) is the author/funder, who has granted bioRxiv a license to display the preprint in perpetuity. It is made available under aCC-BY-NC-ND 4.0 International license.

Supplementary Video 1 Comparison between light sheet (LS) illumination and epi-illumination (Epi) for single-molecule imaging. The movie shows single molecules of Alexa Fluor 647, which were used to label the nuclear lamina protein lamin B1 in a HeLa cell. The fluorophores were imaged using a standard point spread function. Light sheet illumination clearly reduced the background as compared to epi-illumination. The movie is shown at constant contrast and at live speed. Scale bar is 5 µm.

Supplementary Video 2 Single-molecule imaging using a 4-µm Tetrapod point spread function. The movie shows single molecules of Alexa Fluor 647, which were used to label microtubules in a BS-C-1 cell. The fluorophores were imaged using a Tetrapod point spread function with a 4 µm axial range implemented using a deformable mirror. The movie is shown at live speed. Scale bar is 3 µm.

Supplementary Video 3 3D super-resolution reconstruction of microtubules. Movie of reconstruction in **Figure 2a** (right) showing microtubules (α/β-tubulin) in a BS-C-1 cell immunolabeled with Alexa Fluor 647. Imaging of single molecules and fiducial beads was performed with 4-µm and 6-µm Tetrapod point spread functions, respectively, implemented using a deformable mirror.

Supplementary Video 4 3D super-resolution reconstruction of microtubules. Movie of part of the reconstruction in **Figure 2a** (right) showing microtubules (α/β-tubulin) in a BS-C-1 cell immunolabeled with Alexa Fluor 647. Imaging of single molecules and fiducial beads was performed with 4-µm and 6-µm Tetrapod point spread functions, respectively, implemented using a deformable mirror.

Supplementary Video 5 Single-molecule imaging using the double-helix point spread function. The movie shows single molecules of Alexa Fluor 647, which were used to label mitochondria in a HeLa cell. The double-helix point spread function has an axial range of ~2-3 µm and was implemented using a transmissive dielectric phase mask. The movie is shown at live speed. Scale bar is 3 µm.

Supplementary Video 6 3D super-resolution reconstruction of mitochondria. Movie of reconstruction in **Figure 2b** (left) showing mitochondria (TOM20) in a HeLa cell immunolabeled with Alexa Fluor 647. Imaging of single molecules and fiducial beads was performed with the double-helix point spread function implemented using a transmissive dielectric phase mask.

Supplementary Video 7 3D super-resolution reconstruction of mitochondria. Movie of reconstruction in **Figure 2b** (right) showing mitochondria (TOM20) in a HeLa cell immunolabeled with Alexa Fluor 647. Imaging of single molecules and fiducial beads was performed with the double-helix point spread function implemented using a transmissive dielectric phase mask.

Supplementary Video 8 Comparison between light sheet (LS) illumination and epi-illumination (Epi) for 3D single-molecule imaging. The movie shows single molecules of Alexa Fluor 647, which were used to label mitochondria in a HeLa cell. The double-helix point spread function has an axial range of ~2-3 µm and was implemented using a transmissive dielectric phase mask. Light sheet illumination clearly reduces the background as compared to epi-illumination. Statistics from single-molecule localizations from this data set are shown in **Supplementary Figure 10**. The movie is shown at live speed. Scale bar is 5 µm.

Supplementary Video 9 Comparison between **s**ingle-molecule imaging using the double-helix point spread function at the bottom and top (>5 µm above the coverslip) of the nucleus. The movie shows single

bioRxiv preprint doi: https://doi.org/10.1101/135699; this version posted May 9, 2017. The copyright holder for this preprint (which was not certified by peer review) is the author/funder, who has granted bioRxiv a license to display the preprint in perpetuity. It is made available under aCC-BY-NC-ND 4.0 International license.

molecules of Alexa Fluor 647, which were used to label lamin B1 in a HeLa cell. The double-helix point spread function has an axial range of ~2-3 µm and was implemented using a transmissive dielectric phase mask. The movie is shown at live speed. Scale bar is 5 µm.

Supplementary Video 10 3D SR reconstruction of the entire nuclear lamina in a HeLa cell. Movie of reconstruction in **Figure 2d** (left) showing the lamina (lamin B1) in a HeLa cell immunolabeled with Alexa Fluor 647. Imaging of single molecules and fiducial beads was performed with the double-helix point spread function and a 6-µm Tetrapod point spread function, respectively, implemented using transmissive phase masks.

Supplementary Video 11 Sectioning of the entire nuclear lamina in a HeLa cell. Movie showing 100-nm thick z-slices of a 3D SR reconstruction of the entire nuclear lamina (lamin B1) in a HeLa cell immunolabeled with Alexa Fluor 647. Imaging of single molecules and fiducial beads was performed with the double-helix point spread function and a 6-µm Tetrapod point spread function, respectively, implemented using transmissive phase masks.

Supplementary Video 12 3D SR reconstruction of lamin meshwork enveloping an intranuclear channel. Movie of reconstruction in **Figure 2d** (top right) showing a 1.3-µm thick y-slice of the 3D SR reconstruction of the nuclear lamina (lamin B1) in a HeLa cell immunolabeled with Alexa Fluor 647, where the lamin meshwork enveloping an intranuclear channel is visualized. Imaging of single molecules and fiducial beads was performed with the double-helix point spread function and a 6-µm Tetrapod point spread function, respectively, implemented using transmissive phase masks.